PONTIFICIA UNIVERSIDAD CATÓLICA DEL PERÚ

ESCUELA DE POSGRADO

Geometric Phase in Photonics

A thesis in candidacy for the degree of Master of Science in Physics
presented by:

Juan Carlos Loredo Rosillo

Advisor:
Prof. Francisco De Zela

Jury:
Prof. Eduardo Massoni
Prof. Hernán Castillo

Lima, 2011

Geometric Phase in Photonics

Juan Carlos Loredo Rosillo

Propuesto para el Grado de Magíster en Física

Resumen

Las fases geométricas son tema de investigación actual en diversas áreas de la física. Interesa investigarlas tanto por razones de carácter teórico, cuanto por razones ligadas a sus aplicaciones. Entre estas últimas resaltan las aplicaciones en información cuántica. Un computador cuántico está basado en la posibilidad de generar, almacenar y manipular bits de información codificados en los grados de libertad de sistemas cuánticos. Estos son llamados qubits. Los qubits son superposiciones coherentes de dos estados fundamentales. Mientras su contraparte clásica puede valer 0 o 1 excluyentemente, el qubit puede tomar ambos valores 0 y 1 simultaneamente. Esto hace posible procesar información con mucha mayor rapidez en comparación a una computadora clásica. El problema central con los qubits es que son sumamente frágiles, de modo que su tiempo de vida media es muy pequeño. El fenómeno que lleva a un estado de superposición hacia un estado clásico se llama decoherencia. Para que un computador cuántico sea viable, es necesario contar con qubits cuya vida media sea mayor que el tiempo que toma realizar operaciones sobre ellos (computación). Una ruta muy promisoria es la que se basa en las fases geométricas. Ellas permiten realizar operaciones que, de un lado, pueden ser muy rápidas y, de otro lado, pueden ser inmunes o muy robustas frente a la decoherencia. Para implementar computación cuántica geométrica, es entonces necesario ser capaz de manipular fases geométricas con gran versatilidad. Contribuyendo a este fin, esta tesis presenta nuevos resultados en la manipulación de fases geométricas que aparecen cuando el qubit está codificado en fotones polarizados. Esta tesis contiene dos partes principales. En la primera parte hacemos un intento preliminar en manipular fases en estados de polarización. Específicamente, tratamos a la fase de Pancharatnam (fase total) que resulta de evoluciones unitarias arbitrarias. Discutimos los aspectos teóricos involucrados y mostramos en detalle como hacer que un estado de polarización siga cualquier curva sobre la esfera de Poincaré. Luego presentamos los métodos utilizados para llevar a cabo las mediciones de la fase total acumulada a lo largo de la evolución del estado. En la segunda parte de esta tesis, extendemos nuestros métodos y desarrollamos técnicas para suprimir localmente las fases dinámicas que puedan aparecer durante la evolución del estado de polarización. Esto nos permite observar y medir fases geométricas. Usando métodos similares a los discutidos en la primera parte, mostramos finalmente que las fases geométricas observadas experimentalmente coinciden con las predicciones teóricas con buena aproximación.

Geometric Phase in Photonics

Juan Carlos Loredo Rosillo

Presented Towards a Master's Degree in Physics

Abstract

Geometric phases constitute a subject of active research embracing different aspects of physics. The interest comes from both fundamental reasons and applications. Among the latter one should highlight applications in quantum information. Quantum computers are based in the possibility of generating, storing and manipulating bits of information encoded into degrees of freedom of quantum systems. We call them qubits. They are coherent superpositions of two fundamental states. Qubits differ from their classical counterparts for which either 0 or 1 are the only possible values. A qubit can take both values 0 and 1 simultaneously. This makes it possible to process information much faster as compared to classical computers. Such a feature gives a highly superior potential to quantum computers. A main problem with qubits is that typically they are very fragile and their mean life time is very short. The process that turns a coherently superposed state into a single state is called decoherence. In order to make a quantum computer feasible, the mean life time of qubits needs to be larger than the time needed for operating with them. A very promising way to deal with the decoherence problem is based on geometric phases. Using them one should be able to perform operations (with quantum phase gates) that on the one hand could operate very fast and on the other hand should be immune to, or highly robust against, disturbances that usually cause decoherence. In order to implement geometric quantum computation, it is then mandatory that one can manipulate geometric phases with great versatility. As an endeavor towards this direction, this thesis presents some novel experimental results in manipulation of geometric phases appearing when the qubit is encoded in polarization. This thesis contains two major parts. In the first part we make an initial attempt to manipulate phases in polarized states. Specifically, we deal with the Pancharatnam's phase (total phase) arising from arbitrary unitary evolutions. We discuss some theoretical considerations and show in detail how to experimentally bring a polarization state to follow any path on the Poincaré sphere. Then, we present the two methods Polarimetry and Interferometry used to carry out measurements of the accumulated total phase. In the second part of this thesis, we extend our methods by developing techniques to locally suppress dynamical phases that may appear during the evolution of the state of polarization. This allows us to observe and measure geometric phases solely. By using the same two methods discussed in the first part, we then show that our measurements of geometric phases closely fit the theoretical predictions.

Acknowledgements

I am convinced that this small work would have been absolutely impossible if it was not for the intervention of several individuals, with whom I shared in one way or another fragments of my brief time on Earth (that is all that there is!). To all of them, I owe a big and sincere Thank You!

I would like to express my deepest thanks to Noemí Rosillo, my mother, whose unconditional support made the road easier to walk. My father, brother and sister certainly did their part too and I am grateful for that. I am most grateful to Margot Chavez for filling up my life and heart with priceless moments, gracias Gota!

I owe a great debt of thanks to my advisor Professor Francisco De Zela for his academic guidance and support during my studies on this corner of knowledge known as physics. Dankeschön Professor Gerd Leuchs for giving me the opportunity of spending several valuable months at the MPL. Muchas gracias Professor Enrique Solano and Professor Alán Aspuru-Guzik for your key intervention at the final stage of my Masters. Special thanks go to Professor Carlos Monken for his advices during my stay in Belo Horizonte, obrigado por seus ensinamentos!.

To Metin Sabuncu and Onur Danaci, my two best Turkish friends, for giving me your sincere friendship: Teşekkürler dostlarım! Obrigado André Tanus for being family in Minas Gerais, vamos conhecer Machu Picchu ao mesmo tempo cara! I would like to thank my fellow students for the shared moments, specially to Omar Ortiz and Juan Pablo Velásquez. I should not forget to thank David Gilmour and Roger Waters for letting the world be amazed by their brilliant work.

I am sure there are many others that I should have thanked and maybe forgot, thank you all!

Published Material in this Thesis

Partial and final results contained in this thesis work have been published in the following journal articles and proceedings:

J. C. Loredo, O. Ortíz, R. Weingärtner and F. De Zela: "Measurement of Pancharatnam's Phase by Robust Interferometric and Polarimetric Methods", *Phys. Rev. A* **80** 012113 (2009).

J. C. Loredo, O. Ortíz, A. Ballón and F. De Zela: "Measurement of Geometric Phases by Robust Interferometric Methods", *J. Phys.: Conf. Ser.* **274** 012140 (2011).

Contents

List of Figures

Chapter 1

Introduction

Recent experiments have been realized exhibiting geometric phases based on superconducting qubits [1], trapped polarized ultracold neutrons [2] and other spin 1/2 systems [3]. Nevertheless, in all these cases the qubit's evolution was restricted to geodesics or to some specific circuits on the corresponding ray space (Poincaré or Bloch spheres). In contrast, the experiments that will be discussed in this thesis are capable of locally nullifying the dynamical component of the total phase by making it zero at every point of the evolution, thereby ensuring that the accumulated phase is purely geometric.

We should point out that the phenomena studied in this work can be interpreted as pertaining to both the quantum and the classical domain. Even though our experiments were performed using a classical laser source, the mathematical treatment was developed within Dirac's formalism of bra's and ket's and all calculations remain valid for the single-photon case.

We shall now briefly discuss some basic concepts that will be used in this thesis work.

1.1 The Quantum Bit

The smallest unit of information is the bit. This unit can be physically stored in some given system that exists in one of two possible states. For instance, the state of transistor switches in computer processors or the orientation of macroscopic magnetic domains in hard drives.

The qubit is the quantum version of a bit, but unlike its classical counterpart, it can exist in a superposition of two possible quantum states at the same time. Ideally, this qubit is completely isolated, meaning that this two-level system does not interact with the rest of the universe. In real life, however, such condition is not

feasible and thus systems can be used, in which the undesired interactions are weak and become appreciable on time scales much longer than the desired interactions.

1.2 Qubit Encoding using Polarization

For several purposes, photons appear like isolated systems. Polarization encoded qubits have a long decoherence time. Indeed, light from the farthest regions of the observable universe arrive at Earth partially polarized.

For encoding the qubit into the polarization degree of freedom, one assigns the 0 and 1 quantum states to two linearly independent polarization states. We use two orthogonal states and typically take the horizontal $|H\rangle$ and vertical $|V\rangle$ polarizations. Using Dirac's formalism, a pure qubit state in this $\{|H\rangle, |V\rangle\}$ basis is written:

$$|\Psi\rangle = \alpha|H\rangle + \beta|V\rangle, \tag{1.1}$$

with $|\alpha|^2 + |\beta|^2 = 1$, $\alpha, \beta \in \mathbb{C}$. Accordingly, we may rewrite Eq. (1.1) in the form:

$$|\Psi\rangle = e^{i\delta}\left(\cos\frac{\theta}{2}|H\rangle + e^{i\phi}\sin\frac{\theta}{2}|V\rangle\right), \tag{1.2}$$

with $\delta, \theta, \phi \in \mathbb{R}$. The representation in Eq. (1.2) allows the mapping of all single qubit states onto the surface of the unit sphere, with θ and ϕ the polar angles, δ is a global phase factor and is physically irrelevant. This sphere is called the Poincaré sphere and provides a useful tool to vizualise qubits and their evolutions. The linear polarized states lie on the equator and the right and left circular polarized states are located at the north and south poles respectively.

1.2.1 Initialization and Transformations

For fixing a polarization state, out of an initially unknown polarized state, one may use a polarizer (or a polarizing beamsplitter) to project whatever state to a linear state which we may call horizontal or vertical. After this, we can manipulate the state using wave plates that perform unitary evolutions $U \in SU(2)$ acting on single qubits. The wave plates used in experiments come in two types: half wave plates (HWP) and quarter wave plates (QWP). Their matrix representation in the

$\{|H\rangle, |V\rangle\}$ reads:

$$\hat{U}_{HWP}(\theta) = -i \begin{pmatrix} \cos 2\theta & \sin 2\theta \\ \sin 2\theta & -\cos 2\theta \end{pmatrix}, \tag{1.3}$$

$$\hat{U}_{QWP}(\theta) = \frac{1}{\sqrt{2}} \begin{pmatrix} 1 - i\cos 2\theta & -i\sin 2\theta \\ -i\sin 2\theta & 1 + i\cos 2\theta \end{pmatrix}, \tag{1.4}$$

where the angle θ is the angle of the fast axis of the wave plate with respect to the horizontal line.

In Chapters 3 and 4 we make a more detailed analysis of these transformations.

Chapter 2

Phase Fundamentals

Let us think of a quantum system, for instance a polarized photon. Let s be the parameter in terms of which the path of its evolution on the ray space is given. Then this evolution is given by $\rho(s) = |\psi(s)\rangle \langle\psi(s)|$.

When a state $\rho(0) = |\psi(0)\rangle \langle\psi(0)|$ undergoes a cyclic evolution it ends up in $e^{i\varphi} |\psi(0)\rangle \langle\psi(0)| e^{-i\varphi} = \rho(0)$, where it is assumed that the initial and final vector states may differ at most by a phase factor. Since $\rho(s)$ is used to calculate any physical observable it is clear that $|\psi(0)\rangle$ and $e^{i\varphi} |\psi(0)\rangle$ represent the same physical state and no measurement can determine the phase of a single state vector.

However, relative phases between states can be observed, as it was pointed out in 1956 by Pancharatnam [4] when he introduced his definition of relative phase between any two nonorthogonal polarized states. Although Pancharatnam's phase was originally introduced to deal with classical light beams, his definition is still valid in the quantum mechanical scenario, where polarization is an intrinsic property of the photon.

The phase factor φ in $e^{i\varphi} |\psi(0)\rangle$ is composed of two parts: a dynamical phase proportional to the integral of the instantaneous energy and a geometric phase that depends only on the set of states traced out in ray space and not on the rate of evolution. This geometric phase was discovered by Berry but [5] restricted to cyclic and adiabatic evolutions of pure quantum states. It was realized afterwards that such restrictions are not necessary and geometric phases can be found under more general conditions. So, in general it holds:

$$\varphi_{total} = \varphi_{geometric} + \varphi_{dynamical} \tag{2.1}$$

2.1 Pancharatnam's Phase

Pancharatnam's phase was introduced as early as 1956 and anticipated geometric phases. However, it did not receive much attention at that time and had to wait over 30 years, until Berry's paper [6] appeared, in order to be properly appreciated in its importance .

If we ask for the relative phase between $|\psi\rangle$ and $e^{i\varphi}|\psi\rangle$ we know immediately that the answer is φ, but for the general case, i.e. the relative phase between $|\psi_1\rangle$ and $|\psi_2\rangle \neq e^{i\varphi}|\psi_1\rangle$ the definition of relative phase is no longer trivial. This is the case addressed by Pancharatnam, even though he worked in the classical domain of polarization states.

Let us consider two nonorthogonal states $|\Psi_1\rangle$ and $|\Psi_2\rangle$ from the same Hilbert space. Now, inspired on the case of $|\psi\rangle$ and $e^{i\varphi}|\psi\rangle$, the relative phase of $|\Psi_2\rangle$ with respect to $|\Psi_1\rangle$ can be defined as the phase between the normalized component of $|\Psi_2\rangle$ along $|\Psi_1\rangle$ and the original $|\Psi_1\rangle$ state, i.e.:

$$|\Psi_1'\rangle = \frac{|\Psi_1\rangle\langle\Psi_1|\Psi_2\rangle}{|\langle\Psi_1|\Psi_2\rangle|}. \tag{2.2}$$

We can easily see that $\rho_1' = |\Psi_1'\rangle\langle\Psi_1'| = |\Psi_1\rangle\langle\Psi_1| = \rho_1$, and therefore $|\Psi_1'\rangle$ and $|\Psi_1\rangle$ represent the same state. Thus, they differ from one another at most by a phase factor

$$|\Psi_1'\rangle = e^{i\Phi}|\Psi_1\rangle. \tag{2.3}$$

Equation 2.3 leads us to an expression for the relative phase

$$\begin{aligned} e^{i\Phi} &= \langle\Psi_1|\Psi_1'\rangle \\ \Rightarrow \Phi &= \arg\langle\Psi_1|\Psi_1'\rangle \\ \Rightarrow \Phi &= \arg\frac{\langle\Psi_1|\Psi_2\rangle}{|\langle\Psi_1|\Psi_2\rangle|}, \end{aligned} \tag{2.4}$$

since $|\langle\Psi_1|\Psi_2\rangle| \geq 0$ and Φ is the relative phase we are looking for, then

$$\Phi_P = \arg\langle\Psi_1|\Psi_2\rangle. \tag{2.5}$$

Moreover, the difinition in Eq. (2.5) can be realized through the following interferometric recipe. Suppose that $|\Psi_1\rangle$ is submitted to a $U(1)$ shift $e^{i\phi}$. Then, we

make $e^{i\phi}|\Psi_1\rangle$ and $|\Psi_2\rangle$ interfere and the resultant state has the intensity pattern:

$$\begin{aligned} I &= \left|e^{i\phi}|\Psi_1\rangle + |\Psi_2\rangle\right|^2 \\ &\propto 1 + |\langle\Psi_1|\Psi_2\rangle| \cos\left(\phi - \arg\langle\Psi_1|\Psi_2\rangle\right) \ . \end{aligned} \tag{2.6}$$

Maximal interference in Eq. (2.6) will give the relative phase between $|\Psi_1\rangle$ and $|\Psi_2\rangle$. The maxima of I are thus reached for $\phi = \arg\langle\Psi_1|\Psi_2\rangle = \Phi_P$, then

$$\Phi_P = \arg\langle\Psi_1|\Psi_2\rangle \, . \tag{2.7}$$

2.2 Geometric Phases show up

So far, we have presented Pancharatnam's definition of the total relative phase. We can use this definition to see how geometric phases are already on the table. For this purpose we consider Pancharatnam's optical experiment, in which a light beam passes through a set of polarizers, then we ask for the phase between the final and initial state.

Let $|\Psi_0\rangle$ be the initial state, and $|\Psi_k\rangle\langle\Psi_k|, k = 1, ..., N$ the projectors of the N polarizers. The state after the first polarizer is $|\Psi_1'\rangle = |\Psi_1\rangle\langle\Psi_1|\Psi_0\rangle$, after the second polarizer $|\Psi_2'\rangle = |\Psi_2\rangle\langle\Psi_2|\Psi_1'\rangle = |\Psi_2\rangle\langle\Psi_2|\Psi_1\rangle\langle\Psi_1|\Psi_0\rangle$, etc. Then, after N polarizers, the final state will be

$$|\Psi_f\rangle = |\Psi_N\rangle\langle\Psi_N|\Psi_{N-1}\rangle\langle\Psi_{N-1}|\Psi_{N-2}\rangle ... \langle\Psi_2|\Psi_1\rangle\langle\Psi_1|\Psi_0\rangle \, . \tag{2.8}$$

Therefore, the phase between $|\Psi_f\rangle$ and $|\Psi_0\rangle$ is

$$\begin{aligned} \Phi &= \arg\langle\Psi_0|\Psi_f\rangle \\ &= \arg\langle\Psi_0|\Psi_N\rangle\langle\Psi_N|\Psi_{N-1}\rangle\langle\Psi_{N-1}|\Psi_{N-2}\rangle ... \langle\Psi_2|\Psi_1\rangle\langle\Psi_1|\Psi_0\rangle \, . \end{aligned} \tag{2.9}$$

Expressions like the one in Eq. (2.9) are known as Bargmann invariants [7]. Eq.

(2.9) can be put in a more useful form:

$$\begin{aligned}
\Phi &= \arg\langle\Psi_0|\Psi_N\rangle + \sum_{k=1}^{N} \arg\langle\Psi_{N-k+1}|\Psi_{N-k}\rangle \\
&= \arg\langle\Psi_0|\Psi_N\rangle + \sum_{k=1}^{N} \arg\langle\Psi_k|\Psi_{k-1}\rangle \\
&= \arg\langle\Psi_0|\Psi_N\rangle - \sum_{k=1}^{N} \arg\langle\Psi_{k-1}|\Psi_k\rangle \\
\Rightarrow \Phi &= \arg\langle\Psi_0|\Psi_N\rangle - \sum_{k=0}^{N-1} \arg\langle\Psi_k|\Psi_{k+1}\rangle\,. \qquad (2.10)
\end{aligned}$$

At this point we should notice that the phase in Eqs. (2.9) and (2.10) remains unaffected if $|\Psi_k\rangle \to e^{i\phi_k}|\Psi_k\rangle$, i.e. under local $U(1)$ transformations, all dynamical phases cancel in pairs. However, the phase does depend on the set of states the system has passed through.

The phase in Eq. (2.10) was derived from the Pancharatnam's phase between $|\Psi_f\rangle$ and $|\Psi_0\rangle$ for a case in which the evolution is not necessarily unitary. It holds in particular for the unitary evolution, when the $|\Psi_k\rangle$ are intermediate states produced by a unitary operator. In such a case the dynamical phase is not zero in general and it happens to be $\sum_{k=0}^{N-1} \arg\langle\Psi_k|\Psi_{k+1}\rangle$, as we will see in the next section.

Hence, the Pancharatnam and dynamical phases for an arbitrary evolution $|\Phi_k\rangle$, $k = 0, ..., N$ are, respectively:

$$\Phi_P = \arg\langle\Psi_0|\Psi_N\rangle\,. \qquad (2.11)$$

$$\Phi_{dyn} = \sum_{k=0}^{N-1} \arg\langle\Psi_k|\Psi_{k+1}\rangle\,. \qquad (2.12)$$

And, in concordance with Eq. (2.1), the geometric phase $\Phi_g = \Phi_P - \Phi_{dyn}$ reads:

$$\Phi_g = \arg\langle\Psi_0|\Psi_N\rangle - \sum_{k=0}^{N-1} \arg\langle\Psi_k|\Psi_{k+1}\rangle\,. \qquad (2.13)$$

These equations, valid for discrete evolutions, will lead us to the continuous evolution formulas in the next section.

2.3 Quantum Kinematic Approach

Mukunda and Simon [8] developed a framework for dealing with geometric phases based entirely on kinematic ideas. In this section we summarize the most relevant part of their work for our purposes.

Let us consider a Hilbert space $\mathcal{H}$ suitable for the description of a system and a subset $\mathcal{N}_0 \subset \mathcal{H}$ consisting of normalized vectors $|\psi\rangle$:

$$\mathcal{N}_0 = \{|\psi\rangle \in \mathcal{H} \mid \langle\psi|\psi\rangle = 1\} \subset \mathcal{H}. \tag{2.14}$$

Consider now a one-dimensional smooth curve $\mathcal{C}_0 \subset \mathcal{N}_0$ consisting of a family of vectors $|\psi(s)\rangle$:

$$\mathcal{C}_0 = \{|\psi(s)\rangle \in \mathcal{N}_0 \mid s \in [s_1, s_2] \subset \Re\} \subset \mathcal{N}_0. \tag{2.15}$$

We can observe that $\mathcal{N}_0$ remains unchanged under $U(1)$ transformations of $|\psi\rangle$, i.e. $|\psi\rangle \to |\psi'\rangle = e^{i\alpha}|\psi\rangle, \alpha \in \Re$. We can pass now to the corresponding space of equivalence classes, which arises from dividing $\mathcal{N}_0$ with respect to $U(1)$. This is the ray space:

$$\mathcal{R}_0 = \mathcal{N}_0/U(1). \tag{2.16}$$

The curve $\mathcal{C}_0 \subset \mathcal{N}_0$ projects onto a smooth curve $C_0 \subset \mathcal{R}_0$, and so does any other curve $\mathcal{C}_0'$ obtained by applying a gauge transformation $U(1)$ to $\mathcal{C}_0$.

Mukunda and Simon define the geometric phase associated with $\mathcal{C}_0$ as:

$$\begin{aligned} \Phi_g(C_0) &= \arg\langle\psi(s_1)|\psi(s_2)\rangle - \mathrm{Im}\int_{s_1}^{s_2}\langle\psi(s)|\dot{\psi}(s)\rangle\, ds, \\ \Phi_g &= \Phi_{total} - \Phi_{dyn}. \end{aligned} \tag{2.17}$$

This equation can be shown to be related to Eq. (2.10) by using two key results of [8]: there exist curves $\in \mathcal{R}_0$, called geodesics, along which no geometric phase arises; and any two points in ray space can always be connected by a geodesic.

In order to show the connection between Eqs. (2.17) and (2.10) we may consider an open curve $\tilde{C}_0$ made up of N geodesic segments $\tilde{G}_i \subset \mathcal{H}$ connecting $|\Psi_k\rangle, k = 1, ..., N+1$ that project onto geodesics in $\mathcal{R}_0$. Using Eq. (2.17), it holds for the

projection of $\tilde{C}_0$:

$$\begin{aligned}\Phi_g(C_0) &= \Phi_{total}(\tilde{C}_0) - \Phi_{dyn}(\tilde{C}_0) \\ &= \arg\langle\Psi_1|\Psi_{N+1}\rangle - \sum_{k=1}^{N}\Phi_{dyn}(\tilde{G}_k) \\ &= \arg\langle\Psi_1|\Psi_{N+1}\rangle - \sum_{k=1}^{N}\left[\Phi_{total}(\tilde{G}_k) - \Phi_g(\tilde{G}_k)\right], \end{aligned} \tag{2.18}$$

but $\Phi_g(\tilde{G}_k) = 0$, therefore:

$$\Phi_g(C_0) = \arg\langle\Psi_1|\Psi_{N+1}\rangle - \sum_{k=1}^{N}\arg\langle\Psi_k|\Psi_{k+1}\rangle, \tag{2.19}$$

recovering Eq. (2.10).

Another important result is that there is no change of Φ_g if we calculate it either for an open curve $\tilde{C}_0$ or if we close this curve with another segment that projects onto a geodesic in ray space. The last statement becomes evident by noticing that adding a closing element $|\Psi_{N+2}\rangle = |\Psi_1\rangle$ affects Eq. (2.19) in such a way that:

$$\begin{aligned}\arg\langle\Psi_1|\Psi_{N+1}\rangle &\rightarrow \arg\langle\Psi_1|\Psi_{N+2}\rangle \\ &= \arg\langle\Psi_1|\Psi_1\rangle \\ &= 0, \end{aligned} \tag{2.20}$$

and

$$\begin{aligned}-\sum_{k=1}^{N}\arg\langle\Psi_k|\Psi_{k+1}\rangle &\rightarrow -\sum_{k=1}^{N+1}\arg\langle\Psi_k|\Psi_{k+1}\rangle \\ &= -\left(-\arg\langle\Psi_{N+2}|\Psi_{N+1}\rangle + \sum_{k=1}^{N}\arg\langle\Psi_k|\Psi_{k+1}\rangle\right) \\ &= \arg\langle\Psi_1|\Psi_{N+1}\rangle - \sum_{k=1}^{N}\arg\langle\Psi_k|\Psi_{k+1}\rangle, \end{aligned} \tag{2.21}$$

leaving Φ_g unchanged.

We could also go the other way around and derive Eq. (2.17) starting from Eq. (2.19). We can aproximate $\mathcal{C}_0$ by N consecutive segments joining $|\Psi_k\rangle, k = 1, ..., N+1$. As $N \rightarrow \infty$, every two neighboring points $|\Psi_k\rangle$ and $|\Psi_{k+1}\rangle \in \mathcal{C}_0$ will be close enough to approximate such segments by geodesics. In such a case the discrete formula 2.19 leads us to the expression of the geometric phase for the continuous

case, for which we use $|\Psi_1\rangle \to |\psi(s_1)\rangle$, $|\Psi_{N+1}\rangle \to |\psi(s_2)\rangle$ and $|\Psi_{k+1}\rangle \approx |\Psi_k\rangle + \Delta s|\dot{\Psi}_k\rangle$ in[1]:

$$\begin{aligned}
\Phi_g(C_0) &= \lim_{N\to\infty}\left\{\arg\langle\Psi_1|\Psi_{N+1}\rangle - \sum_{k=1}^{N}\arg\langle\Psi_k|\Psi_{k+1}\rangle\right\} \\
&= \lim_{N\to\infty}\left\{\arg\langle\Psi_1|\Psi_{N+1}\rangle - \arg\prod_{k=1}^{N}\langle\Psi_k|\Psi_{k+1}\rangle\right\} \\
&= \lim_{N\to\infty}\left\{\arg\langle\Psi_1|\Psi_{N+1}\rangle - \arg\prod_{k=1}^{N}\langle\Psi_k|\left(|\Psi_k\rangle + \Delta s|\dot{\Psi}_k\rangle\right)\right\} \\
&= \lim_{N\to\infty}\left\{\arg\langle\Psi_1|\Psi_{N+1}\rangle - \arg\prod_{k=1}^{N}\left(1 + \Delta s\langle\Psi_k|\dot{\Psi}_k\rangle\right)\right\} \\
&\approx \lim_{N\to\infty}\left\{\arg\langle\Psi_1|\Psi_{N+1}\rangle - \arg\exp\left(\sum_{k=1}^{N}\langle\Psi_k|\dot{\Psi}_k\rangle\Delta s\right)\right\} \\
&= \arg\langle\psi(s_1)|\psi(s_2)\rangle - \arg\exp\left(i\,\mathrm{Im}\int_{s_1}^{s_2}\langle\psi(s)|\dot{\psi}(s)\rangle\,ds\right) \\
\Rightarrow \Phi_g(C_0) &= \arg\langle\psi(s_1)|\psi(s_2)\rangle - \mathrm{Im}\int_{s_1}^{s_2}\langle\psi(s)|\dot{\psi}(s)\rangle\,ds, \qquad (2.22)
\end{aligned}$$

where we see that, although both Φ_{tot} and Φ_{dyn} are functions defined on $\mathcal{C}_0$; Φ_g, on the other hand, is defined on C_0. This becomes evident when we notice that Φ_g is gauge $U(1)$ invariant. That, if $|\psi(s)\rangle$ is submitted to a $U(1)$ transformation, i.e. $|\psi(s)\rangle \to e^{i\alpha(s)}|\psi(s)\rangle$, Φ_{tot} and Φ_{dyn} change according to:

$$\begin{aligned}
\arg\langle\psi(s_1)|\psi(s_2)\rangle &\to \arg\langle\psi(s_1)|\psi(s_2)\rangle + (\alpha(s_2) - \alpha(s_1))\,, \\
\mathrm{Im}\int_{s_1}^{s_2}\langle\psi(s)|\dot{\psi}(s)\rangle\,ds &\to \mathrm{Im}\int_{s_1}^{s_2}\langle\psi(s)|\dot{\psi}(s)\rangle\,ds + (\alpha(s_2) - \alpha(s_1))\,, \qquad (2.23)
\end{aligned}$$

but Φ_g remais the same.

We will come back to the geometric phase in Chapter 4 with the calculations and results of our experiments.

[1] Upper(lower) case letters are used to denote states for the discrete(continuous) evolution case.

Chapter 3

Pancharatnam's Phase in Photonics

The experiments reported in this thesis [9] were designed to take a pure polarization state, make it evolve unitarily and measure the accumulated phases, either Pancharatnam or geometric, during the evolution. Our phase measurements are largely insensitive to mechanical and thermal disturbances because we came up with a simple idea that makes our interferometer work like an isolated one, without the need to implement a stabilizing system. Such technique can be applied in several types of interferometers, such as variations of Michelson, Sagnac or Mach-Zehnder arrays. We use the latter in our experiments. Let us now take a look at the theoretical calculations related to our experiments.

3.1 General Considerations

In the previous chapter we dealt with the general expression of the Pancharatnam's phase (see Eq. (2.11)). Now we will apply this to a particular case. Here, the pure state we are working with is the polarization of light and we consider only unitary evolutions. Therefore, the polarization space is spanned by the orthonormal basis $\{|H\rangle, |V\rangle\}$ (representing horizontal and vertical polarizations) and the evolution operator $\hat{U}$ is an elements of the $SU(2)$ group.

We introduce two Euler parametrizations for $\hat{U}$, which we call XZX and ZXZ (due to the optical Pauli matrices used to describe them). Each one is more convenient than the other according to the purposes. First, the optical Pauli matrices in

the $\{|H\rangle, |V\rangle\}$ basis are defined as

$$\begin{aligned} \hat{\sigma}_x &= |H\rangle\langle H| - |V\rangle\langle V| \\ \hat{\sigma}_y &= |H\rangle\langle V| + |V\rangle\langle H| \\ \hat{\sigma}_z &= -i\,|H\rangle\langle V| + i\,|V\rangle\langle H|\,. \end{aligned} \tag{3.1}$$

With this definition, the XZX parametrization is given by:

$$\begin{aligned} \hat{U}(\beta,\gamma,\delta) &= \exp\left(i(\frac{\delta+\gamma}{2})\hat{\sigma}_x\right)\exp\left(-i\beta\hat{\sigma}_z\right)\exp\left(i(\frac{\delta-\gamma}{2})\hat{\sigma}_x\right) \\ &= \begin{pmatrix} e^{i\delta}\cos\beta & -e^{i\gamma}\sin\beta \\ e^{-i\gamma}\sin\beta & e^{-i\delta}\cos\beta \end{pmatrix}. \end{aligned} \tag{3.2}$$

Such parametrization easily exhibits Pancharatnam's phase. Indeed, taking as initial state $|i\rangle = |H\rangle$ the final state will be $|f\rangle = \hat{U}(\beta,\gamma,\delta)\,|H\rangle$. Then,

$$\begin{aligned} \Phi_P &= \arg\langle i|f\rangle \\ &= \arg\langle H|\,\hat{U}(\beta,\gamma,\delta)\,|H\rangle \\ &= \arg\left(e^{i\delta}\cos\beta\right) \\ &= \delta + \arg\left(\cos\beta\right), \end{aligned} \tag{3.3}$$

therefore

$$\Phi_P = \begin{cases} \delta & \text{, if } \cos\beta \geq 0 \\ \delta+\pi & \text{, if } \cos\beta < 0. \end{cases} \tag{3.4}$$

We write, more simply, $\Phi_P = \delta$ (modulo π) (experimentally, we measure Φ_P modulo π).

On the other hand, the ZXZ form is given by

$$\hat{U}(\xi,\eta,\zeta) = \exp\left(-i\frac{\xi}{2}\hat{\sigma}_z\right)\exp\left(i\frac{\eta}{2}\hat{\sigma}_x\right)\exp\left(-i\frac{\zeta}{2}\hat{\sigma}_z\right). \tag{3.5}$$

This parametrization is useful for the optical implementation of $\hat{U}$. This is so because any $\hat{U} \in SU(2)$ can be built with three retarders [10], two quarter-wave plates (QWP) and one half-wave plate (HWP). θ_1,θ_2,θ_3 are the arguments of the first, second and third retarder, respectively. We have:

$$\begin{aligned} \hat{Q}(\theta_3)\hat{H}(\theta_2)\hat{Q}(\theta_1) &= \exp\left(-i(\theta_3+3\pi/4)\hat{\sigma}_z\right) \\ &\quad\times\exp\left(i(\theta_1-2\theta_2+\theta_3)\hat{\sigma}_x\right)\exp\left(i(\theta_1-\pi/4)\hat{\sigma}_z\right), \end{aligned} \tag{3.6}$$

where $\hat{Q}$ and $\hat{H}$ are QWP and HWP respectively.

After a comparison between Eqs. (3.5) and (3.6), it is clear how to experimentally implement the ZXZ form:

$$\hat{U}(\xi,\eta,\zeta) = \hat{Q}\left(\frac{-3\pi+2\xi}{4}\right)\hat{H}\left(\frac{\xi-\eta-\zeta-\pi}{4}\right)\hat{Q}\left(\frac{\pi-2\zeta}{4}\right), \tag{3.7}$$

where the argument of a retarder is the angle between the fast axis of the wave plate and the horizontal direction.

3.2 Interferometric Calculations

Wagh and Rakhecha proposed experimental methods to measure Pancharatnam's phase, based on interferometry and polarimetry. In this section we will apply the interferometric one [11] to our case.

In Eq. 2.6 we stated that Pancharatnam's phase may be obtained from general interferometric configurations. Using the XZX and ZXZ representations in our description we obtain for the intensity:

$$\begin{aligned} I &= \left|\frac{1}{\sqrt{2}}\left(e^{i\phi}\left|H\right\rangle + \hat{U}(\beta,\gamma,\delta)\left|H\right\rangle\right)\right|^2 \\ &\propto 1+\cos(\beta)\cos(\phi-\delta), \end{aligned} \tag{3.8}$$

for the XZX case, and

$$\begin{aligned} I &= \left|\frac{1}{\sqrt{2}}\left(e^{i\phi}\left|H\right\rangle + \hat{U}(\xi,\eta,\zeta)\left|H\right\rangle\right)\right|^2 \\ &= 1+\cos\left(\frac{\eta}{2}\right)\cos\left(\frac{\xi+\zeta}{2}\right)\cos(\phi) \\ &\quad +\sin\left(\frac{\eta}{2}\right)\cos\left(\frac{\xi-\zeta}{2}\right)\sin(\phi), \end{aligned} \tag{3.9}$$

for the ZXZ case.

The parameters of one representation can be expressed in terms of the other. On the one hand we have δ, which turns out to be equal to Φ_P (modulo π), on the other hand we have ξ, η and ζ, which are suitable for the experimental implementation. These parameters are related by:

$$\tan(\delta) = \tan\left(\frac{\eta}{2}\right)\frac{\cos\left(\frac{\xi-\zeta}{2}\right)}{\cos\left(\frac{\xi+\zeta}{2}\right)}. \tag{3.10}$$

Furthermore, in our experiments measurements of visibility were also performed. Visibility is defined as:

$$v \equiv \frac{I_{max} - I_{min}}{I_{max} + I_{min}}. \tag{3.11}$$

Although from using Eq. (3.8) in Eq. (3.11) we see that the visibility $v = \cos\beta$ does not depend on Pancharatnam's phase when working with pure states. However, this type of measurements may be useful in experiments with mixed states, in which one extracts from the visibility some information about quantum phases. In terms of the parameters of the ZXZ representation the square of the visibility is given by:

$$v^2(\xi, \eta, \zeta) = \frac{1}{2}\left[1 + \cos\xi\cos\zeta - \cos\eta\sin\xi\sin\zeta\right]. \tag{3.12}$$

Nevertheless, for the experimental implementation it is useful to have Eq. (3.11) written in terms of the angles of the wave plates:

$$\begin{aligned} v^2\left(\theta_1, \theta_2, \theta_3\right) &= \frac{1}{2}[1 + \cos\left(\frac{3\pi + 4\theta_3}{2}\right)\cos\left(\frac{\pi - 4\theta_1}{2}\right) \\ &\quad - \cos\left(2\theta_1 - 4\theta_2 + 2\theta_3\right)\sin\left(\frac{3\pi + 4\theta_3}{2}\right)\sin\left(\frac{\pi - 4\theta_1}{2}\right)] \end{aligned} \tag{3.13}$$

Eqs. (3.8) and (3.9) show the expected output intensity for general interferometric setups. Let us now calculate such expressions specifically for our Mach-Zehnder interferometer, taking into account the contributions of each part of the setup. The Hilbert space is the product space spanned by $\{|H\rangle, |V\rangle\}$ corresponding to the polarization degree of freedom and $\{|X\rangle, |Y\rangle\}$, corresponding to the spatial degrees of freedom, i.e., the two different paths a photon can follow inside the interferometer.

Our interferometric setup is shown in Fig. (3.1). It contains some details that will be explained later on; but let us say now that it mainly consists of a laser beam passing through two beam splitters (BS) and two mirrors (M), and that there is a phase shift in one arm. The operators that represent these elements are [12]:

$$\hat{U}_{BS} = \mathbb{1}_P \otimes \frac{1}{\sqrt{2}}\left(|X\rangle\langle X| + |Y\rangle\langle Y| + i\,|X\rangle\langle Y| + i\,|Y\rangle\langle X|\right), \tag{3.14}$$

$$\hat{U}_{M} = \mathbb{1}_P \otimes \left[-i\left(|X\rangle\langle Y| + |Y\rangle\langle X|\right)\right], \tag{3.15}$$

where $\mathbb{1}_P$ is the identity element of the polarization space. At this point, it is important to note that Eqs. (3.14) and (3.15) are valid whether a quantum or

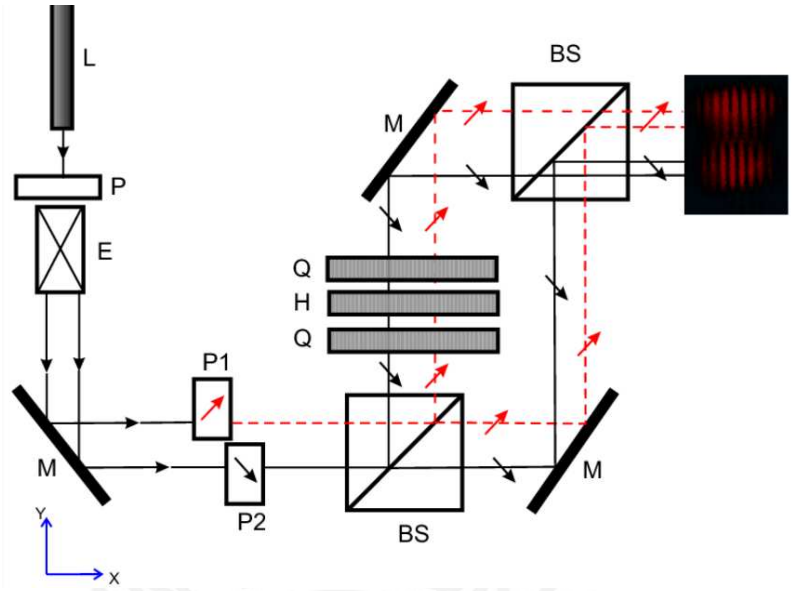

Figure 3.1: Interferometric arrangement for testing Pancharatnam's phase Φ_P. Light from a He-Ne laser (L) passes a polarizer (P)and enters a beam expander (E), after which half of the beam goes through one polarizer (P_1) and the other half goes through a second polarizer (P_2), orthogonally oriented with respect to the first. The two collinear beams feed the same Mach-Zehnder interferometer (BS: beam-splitter, M: mirror), in one of whose arms an array of three retarders has been mounted (Q:quarter-wave plate, H: half-wave plate), so as to realize any desired $SU(2)$ transformation. This transformation introduces a Pancharatnam phase $\Phi_P = \delta$ on one half of the beam and an opposite phase $\Phi_P = -\delta$ on the other, perpendicularly polarized half, so that the relative phase of the two halves equals 2δ. From the relative shift between the upper and lower halves of the interferogram that is captured by a CCD camera set at the output of the array one can determine Φ_P. Any instability of the array affects both halves of the interferogram in the same way, so that the relative shift 2δ is insensitive to instabilities.

classical bit is involved [13]. A phase shift in one or in the other arm is given by:

$$\hat{U}_X(\phi) = \mathbb{1}_P \otimes \left(e^{i\phi} |X\rangle \langle X| + |Y\rangle \langle Y|\right), \tag{3.16}$$

$$\hat{U}_Y(\phi) = \mathbb{1}_P \otimes \left(|X\rangle \langle X| + e^{i\phi} |Y\rangle \langle Y|\right), \tag{3.17}$$

and if we place a transformation $\hat{U} \in SU(2)$, given by an array of three retarders, on arm X or Y of the interferometer, their representations are given by:

$$\hat{U}_P^X = U \otimes |X\rangle \langle X| + \mathbb{1}_P \otimes |Y\rangle \langle Y|, \tag{3.18}$$

$$\hat{U}_P^Y = \mathbb{1}_P \otimes |X\rangle \langle X| + U \otimes |Y\rangle \langle Y|. \tag{3.19}$$

Now, the total action of the Mach-Zehnder in Fig. (3.1) is given by:

$$\hat{U}_{tot} = \hat{U}_{BS}\hat{U}_M\hat{U}_x\left(\phi\right)\hat{U}_P^Y\hat{U}_{BS}. \tag{3.20}$$

Therefore, if we prepare a horizontally polarized beam in the X path, the projector $\hat{\rho}_0 = |HX\rangle\langle HX|$ will describe the system initially ($|HX\rangle \equiv |H\rangle \otimes |V\rangle$). After the interferometer, the polarization-path state is given by $\hat{\rho}_f = \hat{U}_{tot}\hat{\rho}_0\hat{U}_{tot}^\dagger$ and if we put a detector in, say, the X-output, the system collapses to $\hat{\rho}_{pol} = \langle X|\hat{\rho}_f|X\rangle$. Since no polarizer is placed, the final intensity is given by:

$$I = \mathrm{Tr}_{pol}\left[\hat{\rho}_{pol}\right], \tag{3.21}$$

where the trace is taken over the polarization degree of freedom. In a more explicit form:

$$\begin{aligned}
I &= \mathrm{Tr}_{pol}\left[\hat{\rho}_{pol}\right] \\
&= \mathrm{Tr}_{pol}\left[\langle X|\hat{\rho}_f|X\rangle\right] \\
&= \mathrm{Tr}_{pol}\left[\langle X|\hat{U}_{tot}\hat{\rho}_0\hat{U}_{tot}^\dagger|X\rangle\right] \\
&= \langle H|\langle X|\hat{U}_{tot}\hat{\rho}_0\hat{U}_{tot}^\dagger|H\rangle|X\rangle + \langle V|\langle X|\hat{U}_{tot}\hat{\rho}_0\hat{U}_{tot}^\dagger|V\rangle|X\rangle \\
&= \langle HX|\hat{U}_{tot}|HX\rangle\langle HX|\hat{U}_{tot}^\dagger|HX\rangle + \langle VX|\hat{U}_{tot}|HX\rangle\langle HX|\hat{U}_{tot}^\dagger|VX\rangle \\
&= \left|\langle HX|\hat{U}_{tot}|HX\rangle\right|^2 + \left|\langle VX|\hat{U}_{tot}|HX\rangle\right|^2.
\end{aligned} \tag{3.22}$$

A straightforward calculation leads to :

$$\begin{aligned}
I_H &= \frac{1}{2}[1 + \cos\left(\frac{\eta}{2}\right)\cos\left(\frac{\xi+\zeta}{2}\right)\cos\left(\phi\right) \\
&\quad + \sin\left(\frac{\eta}{2}\right)\cos\left(\frac{\xi-\zeta}{2}\right)\sin\left(\phi\right)],
\end{aligned} \tag{3.23}$$

using $\hat{U}$ given in Eq. (3.5), or alternatively:

$$I_H = \frac{1}{2}\left[1 + \cos\left(\beta\right)\cos\left(\phi - \delta\right)\right], \tag{3.24}$$

with $\hat{U}$ given in Eq. (3.2).

In Eqs. (3.23) and (3.24) the intensity is written I_H to indicate that the beam was initially horizontally polarized. At this point we may assume that we have the means to perform measurements of the accumulated phase $\Phi_P = \delta$ when an initial state $|i\rangle = |H\rangle$ evolves to $|f\rangle = \hat{U}(\beta,\gamma,\delta)|H\rangle$. This can be made, e.g., by using a CCD camera as detector and taking a snapshot of the interference pat-

tern when $\hat{U}(\beta,\gamma,\delta) = \mathbb{1}_P$. This will give us an *interferometric pattern* $I_H = \frac{1}{2}[1+\cos(\beta)\cos(\phi)]$. Then, we can set any other $\hat{U}(\beta,\gamma,\delta) \neq \mathbb{1}_P$ and this time we get a second interferometric pattern $I_H = \frac{1}{2}[1+\cos(\beta)\cos(\phi-\delta)]$. By image processing we can obtain the shift of the second pattern with respect to the first (ideally shown in Fig. (3.2)), and having this, a measurement of the total accumulated phase has been done.

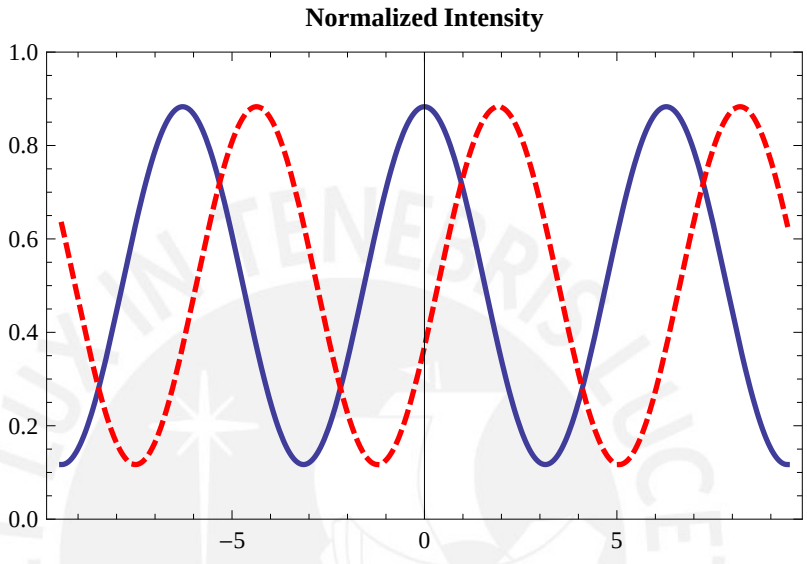

Figure 3.2: Idealized interference profiles after image processing ($\delta = 11\pi/18$): First interferogram with $\hat{U}(\beta,\gamma,\delta) = \mathbb{1}_P$ (straight blue line) and second interferogram with $\hat{U}(\beta,\gamma,\delta) \neq \mathbb{1}_P$ (dashed red line).

What was stated in the last paragraph may look to work fine. At least it does in theory. Nevertheless, it has some experimental hindrances. The main problem with this method is the instability of the interferometer itself. Even tiny vibrations of any component will cause an appreciable drift on the interference patterns, therefore any shift measured will not be due to the evolution of the state alone but to mechanical and thermal disturbances as well. One could counteract this problem by different means. To name some: thermal and mechanical isolation of the entire setup, implementation of a feedback system, or the usage of a Sagnac instead of a Mach-Zehnder interferometer. However, all these methods either complicate the setup or make the measurement process awkward.

Now, some complex problems may have simple solutions. If we could think of a way to make this random extra shift affect both images equally, our problem would be solved, though, without using what was mentioned in the last paragraph, this is impossible for time-separated images. Then, what we need to do is to take two images at the same time, in such a way that we can extract the phase information

from these images.

Now, to finish overcoming our experimental hindrance we may recall that the expression

$$I_H = \frac{1}{2}\left[1 + \cos(\beta)\cos(\phi - \delta)\right] \tag{3.25}$$

arises from considering a horizontally polarized initial state. We may now ask for the intensity when we take a vertically polarized state. This is given by:

$$I_V = \frac{1}{2}\left[1 + \cos(\beta)\cos(\phi + \delta)\right]. \tag{3.26}$$

After a comparison of Eq. (3.25) and (3.26) the solution to our problem is pretty obvious: we should place the two orthogonal polarizations in the same beam (say upper and lower halves orthogonally polarized) having I_H and I_V in the same picture as they will be shifted 2δ one with respect to the other during all the measuring process because all types of perturbations will affect the two halves of the beam equally. Our measurements are therefore insensitive to instabilities and all we need to do is to apply an accurate image processing method to obtain $\Phi_P = \delta$ (modulo π). Such a method should give an accuracy similar to the one reached in polarimetry.

3.3 Polarimetric Calculations

The polarimetric approach to measure Pancharatnam's phase was first proposed by Wagh and Rakhecha [14] for pure states. Others have also proposed similar methods when the state is no longer pure [15]. The polarimetric method is analogous to the interferometric method in the sense that it can be understood as based on *virtual* interference of two states. Below we describe what we mean by this.

First of all, in polarimetry all quantities that we directly measure are intensities. We may now ask for the intensity of the simplest polarimetric array. This is an arrangement in which a laser beam passes through the following steps:

Initial polarizer: it sets an initial linear state.

Unitary transformation: $\hat{U} = \hat{U}(\beta, \gamma, \delta) = \begin{pmatrix} e^{i\delta}\cos\beta & -e^{i\gamma}\sin\beta \\ e^{-i\gamma}\sin\beta & e^{-i\delta}\cos\beta \end{pmatrix}$.

Final polarizer: it projects and measures the final intensity.

Now, considering the polarizers to be aligned along the horizontal/vertical direction,

such setup will result in one of the following intensities:

$$I_{H,H} = \left|\langle H|\hat{U}|H\rangle\right|^2 = \cos^2\beta. \tag{3.27}$$

$$I_{V,H} = \left|\langle V|\hat{U}|H\rangle\right|^2 = \sin^2\beta. \tag{3.28}$$

$$I_{H,V} = \left|\langle H|\hat{U}|V\rangle\right|^2 = \sin^2\beta. \tag{3.29}$$

$$I_{V,V} = \left|\langle H|\hat{U}|H\rangle\right|^2 = \cos^2\beta. \tag{3.30}$$

As we can see, none of the last equations gives us information of $\Phi_P = \delta$, neither will do the usage of any other linear input/output polarizers. Therefore, the question arises: What about considering an elliptically-polarized initial state and an elliptical projector as well? In fact, Wagh and Rakhecha considered a left-circular state, which can be attained by a $\pi/2$ rotation of the $|H\rangle$ state around the y axis of the Poincaré sphere, this is:

$$\begin{aligned} |L\rangle &\equiv \exp\left(-i\frac{\pi}{4}\hat{\sigma}_y\right)|H\rangle \\ &= \frac{1}{\sqrt{2}}\left(|H\rangle - i\,|V\rangle\right). \end{aligned} \tag{3.31}$$

To this state one can apply a phase shift to obtain the elliptical state:

$$\begin{aligned} |E\rangle &\equiv \hat{U}_{shift}(\phi)|L\rangle \\ &= \exp\left(-i\frac{\phi}{2}\hat{\sigma}_x\right)|L\rangle \\ &= \frac{1}{\sqrt{2}}\left(e^{-i\phi/2}\,|H\rangle - ie^{i\phi/2}\,|V\rangle\right) \\ &= \frac{e^{-i\phi/2}}{\sqrt{2}}\left(|H\rangle - ie^{i\phi}\,|V\rangle\right). \end{aligned} \tag{3.32}$$

At this point it has been generated a phase shift ϕ between the components of $|E\rangle$, just like the one between the states in each arm of the interferometer generated by their length difference. Finally, we let the evolution operator U act on $|E\rangle$:

$$\begin{aligned} \hat{U}\,|E\rangle &= \hat{U}\hat{U}_{shift}(\phi)|L\rangle \\ &= \frac{e^{-i\phi/2}}{\sqrt{2}}\left(\hat{U}\,|H\rangle - ie^{i\phi}\hat{U}\,|V\rangle\right). \end{aligned} \tag{3.33}$$

Up to an irrelevant global phase factor, the state in Eq. (3.33) looks pretty much like the one in (3.8). Now it is clear the analogy to the interferometric technique: While in the interferometric approach we make the states $e^{i\phi}\,|H\rangle$ and $\hat{U}(\beta,\gamma,\delta)|H\rangle$

interfere, in the polarimetric approach the components of $\frac{1}{\sqrt{2}}\left(\hat{U}\left|H\right\rangle - ie^{i\phi}\hat{U}\left|V\right\rangle\right)$ are the ones that *virtually* interfere.

The intensity now arises from squaring the projection of $\hat{U}|E\rangle$ on $|E\rangle$:

$$I = \left|\langle E|\hat{U}|E\rangle\right|^2. \tag{3.34}$$

A straightforward calculation taking $\hat{U}$ as given by Eq. (3.2) leads us to:

$$I = \cos^2(\beta)\cos^2(\delta) + \sin^2(\beta)\cos^2(\gamma+\phi). \tag{3.35}$$

It is from this latest equation that we can extract the Pancharatnam's phase. Indeed, we notice from Eq. (3.35) that the minimal and maximal values of I with respect to ϕ are given by:

$$I_{\min} = \cos^2(\beta)\cos^2(\delta), \tag{3.36}$$
$$I_{\max} = \cos^2(\beta)\cos^2(\delta) + \sin^2(\beta). \tag{3.37}$$

Therefore, solving for $\cos^2(\delta)$ in Eqs. (3.36)-(3.37) we can measure $\Phi_P = \delta$ (modulo π) by:

$$\cos^2(\delta) = \frac{I_{\min}}{1 - I_{\max} + I_{\min}}. \tag{3.38}$$

In order to obtain I as given by Eq. (3.35) the following transformations are involved:

$$\begin{aligned} I &= \left|\langle H|\,\hat{U}_{tot}\,|H\rangle\right|^2, \\ &= \left|\langle H|\exp\left(i\frac{\pi}{4}\hat{\sigma}_y\right)\exp\left(i\frac{\phi}{2}\hat{\sigma}_x\right)U\exp\left(-i\frac{\phi}{2}\hat{\sigma}_x\right)\exp\left(-i\frac{\pi}{4}\hat{\sigma}_y\right)|H\rangle\right|^2 \end{aligned} \tag{3.39}$$

Now we want to find the array of retarders that generates the operators mentioned above. For this, we may recall that:

$$\hat{Q}(\alpha) = \exp\left(-i\frac{\pi}{4}\left(\cos(2\alpha)\hat{\sigma}_x + \sin(2\alpha)\hat{\sigma}_y\right)\right), \tag{3.40}$$
$$\hat{H}(\alpha) = \exp\left(-i\frac{\pi}{2}\left(\cos(2\alpha)\hat{\sigma}_x + \sin(2\alpha)\hat{\sigma}_y\right)\right). \tag{3.41}$$

From Eqs. (3.40) and (3.41) we find:

$$\exp\left(-i\frac{\pi}{4}\hat{\sigma}_y\right) = \hat{Q}\left(\frac{\pi}{4}\right), \tag{3.42}$$

$$\exp\left(-i\frac{\phi}{2}\hat{\sigma}_x\right) = \hat{Q}\left(\frac{\pi}{4}\right)\hat{H}\left(\frac{\phi-\pi}{4}\right)\hat{Q}\left(\frac{\pi}{4}\right), \tag{3.43}$$

$$\exp\left(+i\frac{\phi}{2}\hat{\sigma}_x\right) = \hat{Q}\left(\frac{-\pi}{4}\right)\hat{H}\left(\frac{\phi+\pi}{4}\right)\hat{Q}\left(\frac{-\pi}{4}\right). \tag{3.44}$$

Using $\hat{Q}^2\left(\frac{\pi}{4}\right) = \hat{H}\left(\frac{\pi}{4}\right)$ we obtain:

$$\hat{U}_{tot} = \hat{H}\left(-\frac{\pi}{4}\right)\hat{H}\left(\frac{\phi+\pi}{4}\right)\hat{Q}\left(-\frac{\pi}{4}\right)\hat{U}\hat{Q}\left(\frac{\pi}{4}\right)\hat{H}\left(\frac{\phi-\pi}{4}\right)\hat{H}\left(\frac{\pi}{4}\right). \tag{3.45}$$

It was already discussed in section (3.2) that the ZXZ form is suitable for the optical implementation of $\hat{U}$. This becomes explicit in Eq. (3.7). Now, using $\hat{U} = \hat{Q}\hat{H}\hat{Q}$ in Eq. (3.45) we end up with a total of nine wave plates to implement $\hat{U}_{tot}$.

Since we observe that four parameters determine the angles of nine wave plates we expect this array to be reducible. Indeed, we can use the following relations:

$$\hat{Q}(\alpha)\hat{H}(\beta) = \hat{H}(\beta)\hat{Q}(2\beta-\alpha), \tag{3.46}$$

$$\hat{Q}(\alpha)\hat{H}(\beta)\hat{H}(\gamma) = \hat{Q}\left(\alpha+\frac{\pi}{2}\right)\hat{H}\left(\alpha-\beta+\gamma-\frac{\pi}{2}\right), \tag{3.47}$$

to find the reduced array of five retarders that implements $\hat{U}_{tot}$:

$$\begin{aligned}\hat{U}_{tot} = {} & \hat{Q}\left(-\frac{3\pi}{4}-\frac{\phi}{2}\right)\hat{Q}\left(-\frac{5\pi+2\xi}{4}-\frac{\phi}{2}\right)\hat{Q}\left(-\frac{9\pi+2(\xi+\eta)}{4}-\frac{\phi}{2}\right) \\ & \times\hat{H}\left(-\frac{7\pi+\xi+\eta-\zeta}{4}-\frac{\phi}{2}\right)\hat{Q}\left(-\frac{\pi}{4}-\frac{\phi}{2}\right),\end{aligned} \tag{3.48}$$

where we observe that the array has been found in such a way that all the retarders have a common term $\phi/2$, so one could use some mechanical apparatus to rotate the entire setup of five wave plates simultaneously, spanning all the values of I as a function of ϕ. Such an array is shown schematically in Fig. (3.3). The intensity in terms of ξ, η, ζ and ϕ is given by:

$$\begin{aligned} I &= \left|{}_z\langle +|\,\hat{U}_{tot}\,|+\rangle_z\right|^2 \\ &= \cos^2\left(\frac{\eta}{2}\right)\cos^2\left(\frac{\xi+\zeta}{2}\right) \\ &\quad + \left[\cos\left(\frac{\eta}{2}\right)\sin\left(\frac{\xi+\zeta}{2}\right)\cos(\phi) + \sin\left(\frac{\eta}{2}\right)\sin\left(\frac{\xi-\zeta}{2}\right)\sin(\phi)\right]^2. \end{aligned} \tag{3.49}$$

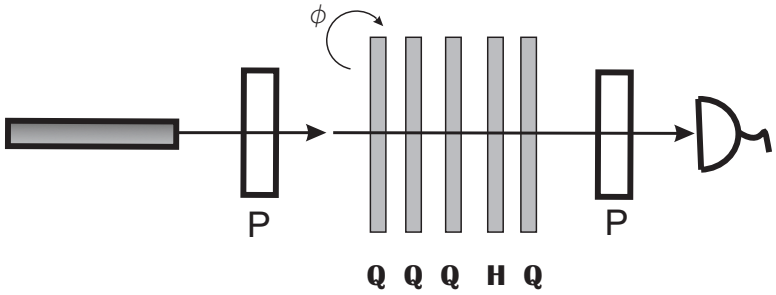

Figure 3.3: Polarimetric arrangement for testing Pancharatnam's phase Φ_P. With an array of five retarders (Q:quarter-wave plate, H: half-wave plate) and two polarizers (P) a relative phase ϕ between two polarization components $|H\rangle$ and $|V\rangle$ can be introduced, on which any desired $SU(2)$ transformation can be applied. The five retarders are simultaneously rotated, thereby varying ϕ, and the intensity $I(\phi)$ is recorded. From the maximum and minimum values of I one can determine Φ_P, according to $\cos^2(\Phi_P) = I_{\min}/(1 - I_{\max} + I_{\min})$.

With this array of five wave plates we can already extract the Pancharatnam's phase from Eq. (3.38) taking I as given by Eq. (3.49). On the other hand, for simplicity we may consider first some particular cases of $\hat{U}_{tot}$, aiming to reduce the number of retarders to simplify the experimental work.

In our first reduced array we set $\zeta = 2\pi$. In such a case Eq. (3.48) reduces to:

$$\hat{U}_{tot}^{\zeta=2\pi} = \hat{Q}(\phi)\,\hat{Q}\left(-\frac{\xi}{2}+\phi\right)\hat{H}\left(\frac{\eta-\xi}{4}+\phi\right), \tag{3.50}$$

where we have redefined $(-3\pi - 2\phi)/4 \to \phi$, and from Eq. (3.38):

$$\cos^2(\delta) = \cos^2(\eta/2), \tag{3.51}$$

for all ξ. Therefore, the Pancharatnam's phase (modulo π) turns out to be:

$$\Phi_P = \eta/2. \tag{3.52}$$

If we instead fix $\xi = -\pi$, $\hat{U}_{tot}$ simplifies to:

$$\hat{U}_{tot}^{\xi=-\pi} = \hat{Q}\left(\frac{3\pi+2\eta-2\phi}{4}\right)\hat{H}\left(\frac{-4\pi+\zeta+\eta-2\phi}{4}\right)\hat{Q}\left(\frac{-\pi-2\phi}{4}\right). \tag{3.53}$$

From Eq. (3.38) we find that:

$$\cos^2(\delta) = \cos^2(\eta/2), \tag{3.54}$$

still holds valid, this time for all ζ, and again:

$$\Phi_P = \eta/2. \tag{3.55}$$

The intensity in this particular case is given by:

$$I = \cos^2\left(\frac{\zeta}{2}\right)\cos^2\left(\frac{\eta - 2\phi}{2}\right) + \sin^2\left(\frac{\zeta}{2}\right)\cos^2\left(\frac{\eta}{2}\right). \tag{3.56}$$

From Eq. (3.56) we observe that $\eta = 0, \zeta = \pi$ will result in a constant value for I, which is useful for adjusting the setup[1].

The experimental measurements of the Pancharatnam's phase Φ_P and the visibility v will be discussed in the following section.

3.4 Experimental Procedures

We have performed measurements of the Pancharatnam's phase by applying the polarimetric and interferometric methods discussed in the previous section. In both cases we have used a 30 mW cw He-Ne laser (632.8 nm) as the light source.

3.4.1 Interferometric Measurements

We used two interferometric arrangements. One of them was a Mach-Zehnder interferometer and the other was a Sagnac interferometer. We started by mounting both interferometers in the standard way, but adding an array of three retarders on one arm for implementing any desired $U \in SU(2)$.

Usually, phase shifts ϕ, as appearing in Eq. (3.8), originated from moving one mirror with, e.g., a low-voltage piezotransducer. One can then record the interference pattern by sensing the light intensity with a photodiode set at one of the output ports of the exiting beam splitter. Alternatively, one can capture the whole interference pattern with a charge-coupled device (CCD) camera. The Mach-Zehnder interferometer is easier to mount in comparison to the Sagnac interferometer. However, it has the disadvantage of being more unstable against environmental disturbances, thus requiring the application of some stabilizing technique such as, e.g., a feedback system. In contrast, the Sagnac interferometer is very stable with respect to mechanical and thermal disturbances. Nevertheless, mounting a Sagnac interferometer was not very useful for our purposes due to some geometrical reasons[2].

[1] One has an idea of how well aligned the setup is depending on how constant I results when varying ϕ.

[2] In the interferometric setup we need U to act on one of the arms of the interferometer. On the

By using one or the other method, one can obtain two interferograms – one with $U = \mathbb{1}_P$ and the other with $U \neq \mathbb{1}_P$–. In our case, capturing the whole interference pattern with a CCD camera – instead of sensing it with a photodiode – proved to be the most convenient approach with both arrangements, Mach-Zehnder and Sagnac.

When working with the Mach-Zehnder array, we first implemented a feedback system in order to stabilize the reference pattern. One of the two paths followed by the laser beam was used for feedback. The feedback system should allow us to compensate the jitter and thermal drifts of the fringe patterns that preclude a proper measurement of the phase shift. The feedback system requires an electronic signal, after proportional-integral amplification, to be fed into a piezotransducer within a servoloop, so as to stabilize the interferometer, thereby locking the fringe pattern. Although we succeeded in locking the fringe patter, the geometry of our array severely limited the parameter range we could explore. We thus turned to a different option, i.e., the one based on Eqs. (3.25) and (3.26). It required polarizing one half of the laser beam in one direction and the other half in a direction perpendicular to the first one.

In order to exhibit the feasibility of our interferometric method, we performed experiments with both Mach-Zehnder and Sagnac arrays. In both cases we obtained similar preliminary results. However, the systematic recording of our results corresponds to the Mach-Zehnder array shown in Fig. (3.1), as it was the simpler one to mount and manipulate.

As shown in Fig. (3.1), the initially polarized laser beam was expanded, so that its upper half passed through one polarizer P_1 and its lower half through a second polarizer P_2 orthogonally oriented with respect to the first. Each run started by setting the retarders so as to afford the identity transformation: $Q(\pi/4)H(-\pi/4)Q(\pi/4) = \mathbb{1}_P$, the corresponding interferogram was captured with a CCD camera ($1/4''$ Sony CCD, video format of 640×480 pixels, frame rate adjusted to 30 fps) and digitized with an IBM -compatible computer.

The upper and lower halves of this interferogram showed a small relative shift stemming from surface irregularities and tiny misalignments. The initial interferogram served to gauge all the successive ones that correspond to transformations $U(\xi, \eta, \zeta) \neq \mathbb{1}_P$. Each interferogram was evaluated with the help of an algorithm that works as follows. First, by optical inspection of the whole set of interferograms -corresponding to a given $U(\xi, \eta, \zeta)$- one selects (by pixel numbers) a common region R_0 of the images the algorithm should work with (see Fig.(3.4)).

Having this region as its input the algorithm performs a column average of each

other hand, in the Sagnac interferometer both states trace the same path. Therefore they cross the same wave plates that implement U.

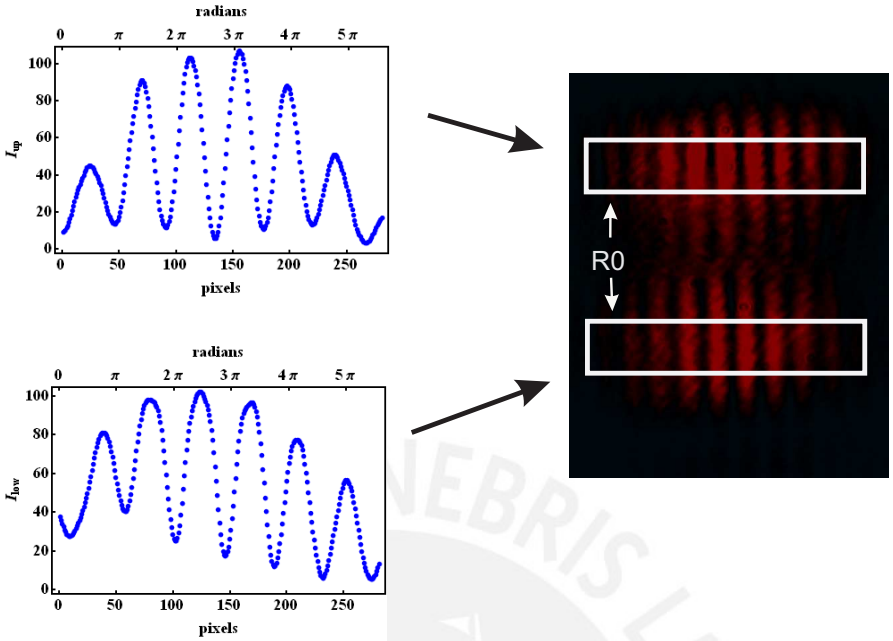

Figure 3.4: Pancharatnam's phase can be extracted from the relative fringe-shift between the upper and lower parts of the interferogram. The relative shift equals twice the Pancharatnam's phase. The left panels show the result of performing a column average of the fringes plus the application of a Savitzky-Golay filter to get rid of noise features. The column average is performed after selecting the evaluation area R_0 on the interferogram, as illustrated on the right panel. The reported shifts are mean values obtained from four different selections, $R_0, \ldots, R_3$, of the evaluation area.

half of the interferogram – thereby obtaining the mean profile of the fringes – and the output is then submitted to a low-pass filter (Savitzky-Golay filter) to get rid of noisy features. The result is a pair of curves like those shown in Fig. (3.4). The algorithm then searches for relative minima in each of the two curves and compares their locations so as to output the relative shifts between the minima of the curves. After averaging these relative shifts the algorithm produces its final output for each pair of curves. We repeated this procedure for a series of regions (fixed by pixel numbers): $R_0 \ldots R_3$, so that we could estimate the uncertainty of our experimental values.

No attempt was made to automate the selection of the working regions. Visual inspection proved to be effective enough for our present purposes. Some series of interferograms showed limited regions that were clearly inappropriate for being submitted to evaluation, as they reflected inhomogeneities and other features that

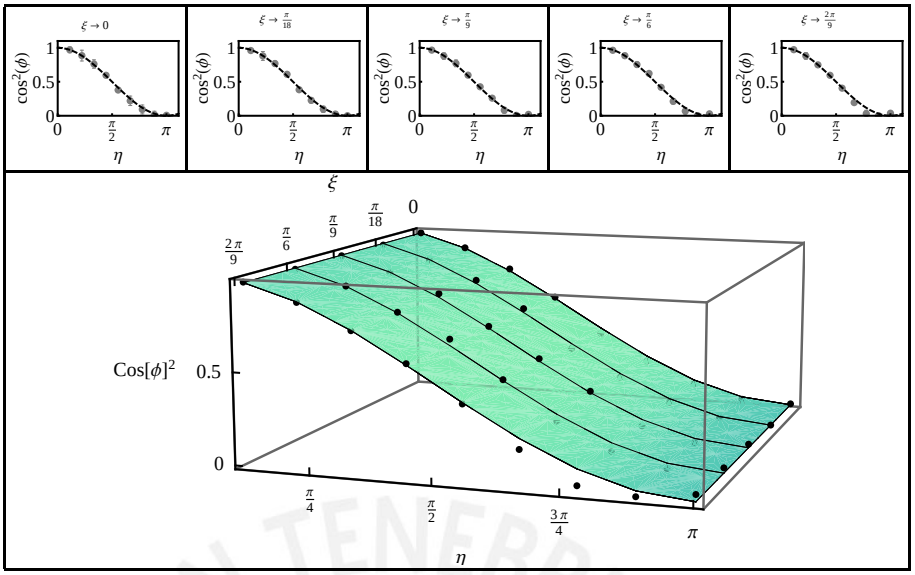

Figure 3.5: Experimental results from the interferometric measurement of Pancharatnam's phase. We plot $\cos^2(\Phi_P)$ as a function of ξ and η, with ζ being held fixed to zero. In the upper panels we plot the single curves that are highlighted on the surface shown on the lower panel. Dots correspond to experimental values, some of which fall below and some above the surface.

stemmed from surface irregularities of the optical components. We applied the complete procedure to a whole set of interferograms corresponding to different choices of $U(\xi, \eta, \zeta)$. Our results are shown in Fig. (3.5). As can be seen, our experimental results are in very good agreement with theoretical predictions.

A second, independent, algorithm was also used to check the above results. This algorithm was developed as a variant of some commonly used procedures in image processing. Like in the previous approach, the algorithm first constructs the mean profiles of the fringes and submits them to a low-pass filter. But now, instead of searching for relative minima, the algorithm does the following. First, it determines the dominant spatial carrier frequency k_0 by Fourier transforming curves like those shown in Fig. (3.4). Let us denote these curves by $\widehat{i}_{up}(x)$ and $\widehat{i}_{low}(x)$, corresponding, respectively, to the upper and lower half of the interferogram. The Fourier transforms are denoted by $i_{up}(k)$ and $i_{low}(k)$. The goal is to determine the relative shift $\Delta_r = 2\delta$ between $\widehat{i}_{up}(x)$ and $\widehat{i}_{low}(x)$. It can be shown [16] that $\Delta_r = \Delta_{up} - \Delta_{low} \approx \mathrm{Im}[\log(i_{up}(k_0))] - \mathrm{Im}[\log(i_{low}(k_0))]$, up to a constant phase-offset that is the same for all the interferograms pertaining to a given $U(\xi, \eta, \zeta)$.

The above expression for Δ_r comes from observing that both $i_{up}(k_0)$ and $i_{low}(k_0)$ have the structure $i(k_0) = a(k_0) + b(0)\exp(i\Delta) + b^*(2k_0)\exp(-i\Delta)$, so that $i(k_0) \approx b(0)\exp(i\Delta)$ whenever $|b(0)| \gg |b^*(2k_0)|$, $|a(k_0)|$. Thus, the accuracy of the approx-

imation for Δ_r depends on how well one can separate the Fourier components of $i(k_0)$. In the present case we applied this procedure only for the sake of checking our results. An attempt to systematize this method would be worth only if one's goals require an automated phase-retrieval method. In our case, as we were interested in giving a proof of principle only, the method of choice was not a fully automated one, but a partially manual method which was envisioned to demonstrate the feasibility of our approach.

Another series of tests was devoted to measuring the visibility v as given in Eq. (3.13). The quantity $v(\theta_1, \theta_2, \theta_3)$ was submitted to test by fixing two of its three arguments. Our results are shown in Fig. (3.6). The left panels correspond to $v(\theta_1, \theta_2, \theta_3)$ as a function of θ_2 and θ_3, that is, the surface obtained by fixing θ_1 as indicated. In the right panels we compare the theoretical predictions against our measurements of $v(\theta_1, \theta_2, \theta_3)$, whereby two of the three arguments have been held fixed. The interferograms were evaluated following a procedure similar to the one already explained. However, in this case it was not the full cross section of the beam that was submitted to evaluation, but a manually chosen region of the images corresponding to a part of the input beam having almost uniform intensity. This had to be so, because Eq. (3.13) presupposes a uniform profile of the input beam. In order to test the visibility of the whole cross section of the beam, Eq. (3.13) should be modulated with a Gaussian envelope. Such a refinement was however unnecessary for our scopes. In any case, the experimental value of the visibility, $v \equiv (I_{max} - I_{min})/(I_{max} + I_{min})$, was obtained by choosing in each interferogram several maxima and minima, so as to assess the accuracy of our measurements. Thus, the error bars in the figures take proper account of the tiny variations in the chosen region of the input-beam profile. As can be seen, the experimental values closely fit the theoretical predictions.

3.4.2 Polarimetric Measurements

The polarimetric arrangement shown in Fig. (3.3) could have been designed so that the five retarders (see Eq. (3.48)) could be simultaneously rotated by the same amount. If one aims at systematically measuring Pancharatnam's phase with the polarimetric method, this would require having a custom-made apparatus on which one can mount the five plates with any desired initial orientation and then submit the whole assembly to rotation.

As our aim was to simply exhibit the versatility of the method and to compare its accuracy with that of the interferometric method, we mounted a simple array of five independent retarders so that each one of them could be manually rotated.

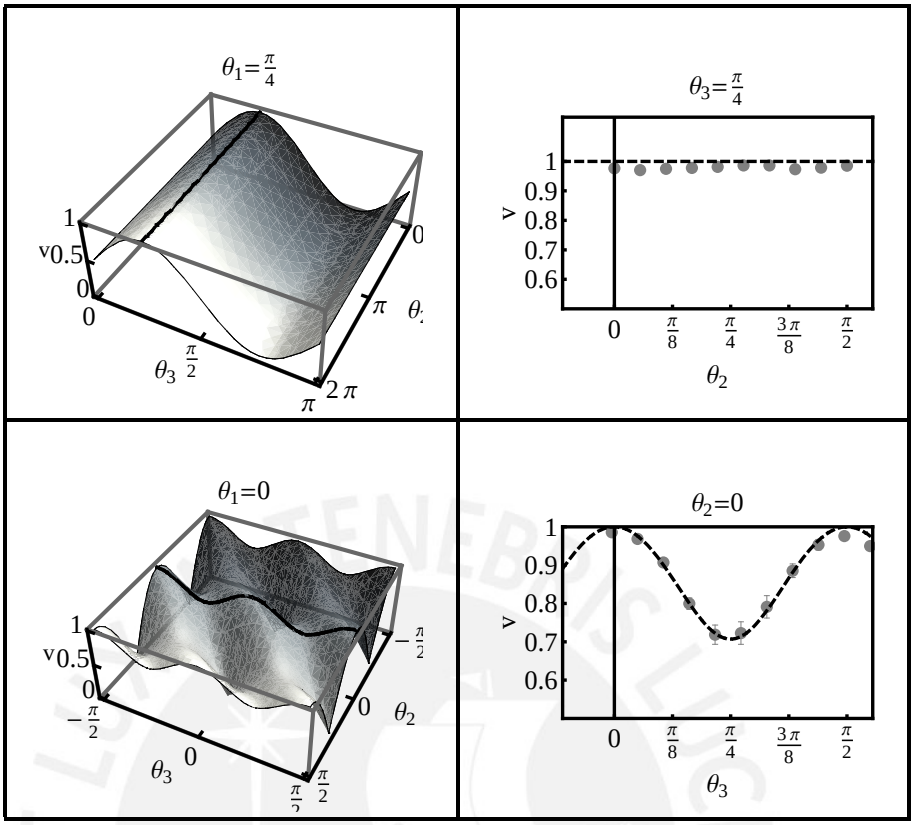

Figure 3.6: Interferometric measurement of the visibility $v(\theta_1, \theta_2, \theta_3)$. The left panels show the surfaces obtained by fixing one of the three angles, θ_1, as indicated. The right panels show the experimental results that correspond to the curves highlighted on the surfaces. The upper curve is obtained by fixing θ_3 besides θ_1, the lower curve by fixing θ_2 and θ_1. In the upper curve all experimental values fall below the predicted (maximal) visibility of 1. This is because I_{min} is never zero, as required to obtain $v = 1$. By subtracting the nonzero average of I_{min} the experimental points would fall above and below the theoretical curve, as it occurs for the lower curve, which corresponds to $v < 1$.

With such an approach it takes some hours of painstaking manipulation to record all necessary data, whenever the experiment is performed with the full array of five retarders. For this reason, we initially restricted our tests to three retarders as already mentioned. This could be achieved by lowering the degrees of freedom, i.e., by fixing one of the three Euler angles, as explained in the previous section (see Eqs. (3.50), (3.53)). Having made measurements with three plates we performed an additional run of measurements with the full arrangement of five retarders.

Our results are shown in Fig. (3.7). As expected (retarders and polarizers could be oriented to within 1^0), the experimental values are within 3-6% in accordance with the theoretical predictions, depending on the number of retarders being employed.

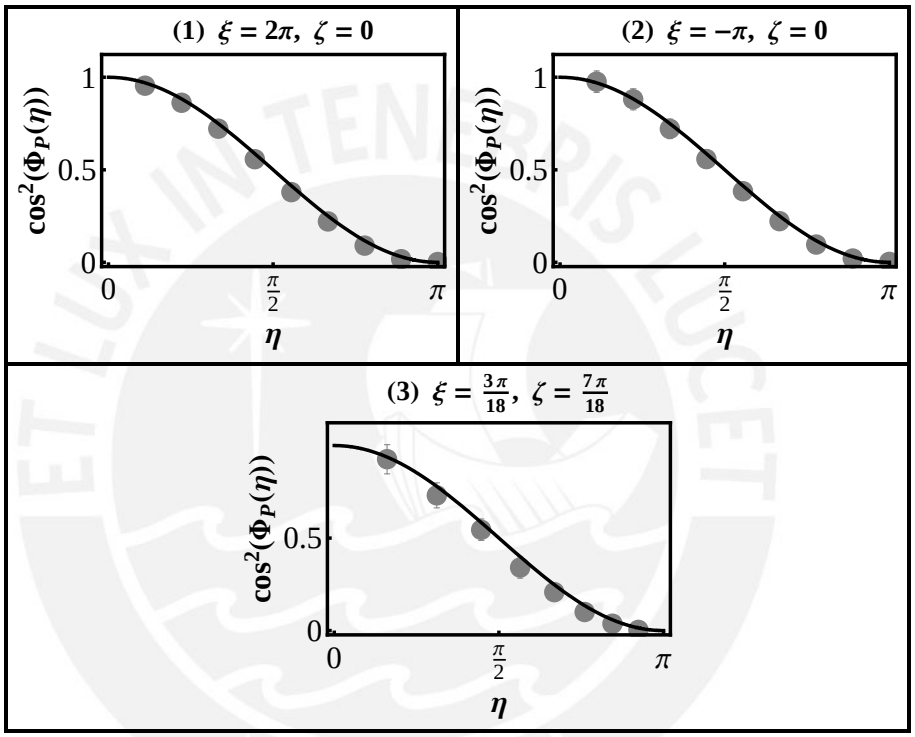

Figure 3.7: Experimental results from a polarimetric measurement of Pancharatnam's phase. The upper graphs correspond to an array that consists of three retarders set in the form QQH (left) and QHQ (right). Parameter values are as indicated and $\cos^2(\Phi_P)$ was measured as a function of η. The lower curve corresponds to the full array of five retarders set in the form $QQQHQ$.

Chapter 4

Geometric Phase in Photonics

The Pancharatnam's phase associated to any evolution accounts for all the contributions to the accumulated phase, including dynamical factors such as rates of evolution. Geometric phases, on the other hand, are completly determined by geometric properties. For instance, the geometric phase acquired in any closed curve on the Poincaré sphere is proportional to the solid angle enclosed by such a curve.

Several works have been devoted to geometric phases. Some are theoretical and aim at a better understanding of this phenomenon. To name a few: geometric phases in orthogonal states [17], in mixed states [18], quantum computation based on geometric phases [19], noise on geometric logic gates [20] and geometric manipulation of trapped ions [21]. Experimental work refers to: observation of geometric phases in classical states of light [22], in mixed states [23], in nuclear magnetic resonance [24], or experimental demostrations of geometric quantum gates [25], [26]. In this chapter we discuss the manipulation of geometric phases that appear when the qubit is carried by a polarized photon.

4.1 General Considerations

After measuring Pancharatnam phase our work focussed on geometric phases in photonics, where similar techniques to those explained in Chapter 3 were used and some others were added. In this chapter we will show how to make a polarization state of light trace an arbitrary path on the Poincaré sphere, as shown schematically in Fig. 4.1, in such a way that the dynamical component of the Pancharatnam's phase gained during each step of the evolution vanishes, leaving an accumulated phase that is purely geometric.

Let us now turn to the mathematical description of our problem. Following Section 2.3, given a smooth curve $\mathcal{C}_0$ described by $|\psi(s)\rangle, s \in [s_1, s_2]$ in the state

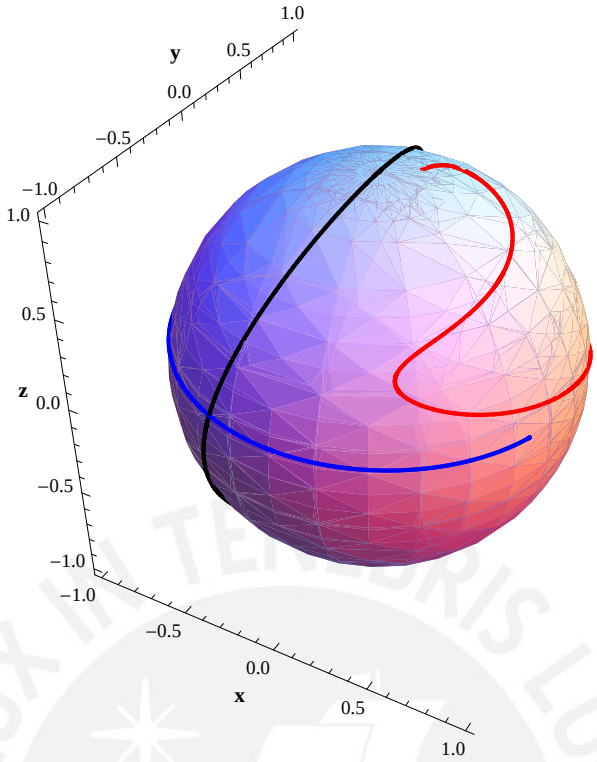

Figure 4.1: Arbitrary paths over the Poincaré sphere. Curves $\mathcal{C}_0$ and $\widetilde{\mathcal{C}}_0$, given by $|\psi(s)\rangle$ and $e^{i\alpha(s)}|\psi(s)\rangle$ respectively, project both onto the same C_0 in the ray space.

space, which projects on another curve C_0 that is described by $|\psi(s)\rangle\langle\psi(s)|$ in the ray space, the geometric phase Φ_g acquired by $|\psi(s)\rangle$ is:

$$\begin{aligned}\Phi_g(C_0) &= \Phi_P(\mathcal{C}_0) - \Phi_{dyn}(\mathcal{C}_0) \\ &= \arg\langle\psi(s_1)|\psi(s_2)\rangle - \mathrm{Im}\int_{s_1}^{s_2} \arg\langle\psi(s)|\dot{\psi}(s)\rangle\, \mathrm{d}s. \end{aligned} \tag{4.1}$$

We may now recall that Φ_g is a gauge $U(1)$ invariant, i.e., it remains unchanged

under $|\psi(s)\rangle \to |\widetilde{\psi}(s)\rangle = e^{i\alpha(s)}|\psi(s)\rangle$:

$$\begin{aligned}
\widetilde{\Phi}_g &= \widetilde{\Phi}_P(\widetilde{\mathcal{C}}_0) - \widetilde{\Phi}_{dyn}(\widetilde{\mathcal{C}}_0) \\
&= \arg\langle\widetilde{\psi}(s_1)|\widetilde{\psi}(s_2)\rangle - \mathrm{Im}\int_{s_1}^{s_2}\langle\widetilde{\psi}(s)|\dot{\widetilde{\psi}}(s)\rangle\,\mathrm{d}s \\
&= \arg\langle\psi(s_1)|\psi(s_2)\rangle + (\alpha(s_2)-\alpha(s_1)) \\
&\quad - \mathrm{Im}\int_{s_1}^{s_2}\langle\psi(s)|\dot{\psi}(s)\rangle\,\mathrm{d}s - (\alpha(s_2)-\alpha(s_1)) \\
&= \arg\langle\psi(s_1)|\psi(s_2)\rangle - \mathrm{Im}\int_{s_1}^{s_2}\langle\psi(s)|\dot{\psi}(s)\rangle\,\mathrm{d}s \\
&= \Phi_P(\mathcal{C}_0) - \Phi_{dyn}(\mathcal{C}_0) \\
&= \Phi_g, \qquad (4.2)
\end{aligned}$$

This fact can be exploited to make the dynamical phase vanish at each point of the evolution. We can achieve this by an appropriate choice of the gauge. That is, $\Phi_{dyn} = 0$ is fulfilled when $\alpha(s)$ is chosen such that:

$$\mathrm{Im}\langle\psi(s)|\dot{\psi}(s)\rangle + \dot{\alpha}(s) = 0. \qquad (4.3)$$

In chapter 3 we chose to use two different representations to describe the evolution operators, one of which allowed us to easily handle the experimental implementation while the other had one of its parameters equal to Φ_P. Instead of that, from now on we will make our calculations using another parametrization, this time suitable for identifying the specific path followed by the state on the Poincaré sphere during its evolution. Such parametrization will be determined by the axis $\vec{n}(\theta_n, \phi_n)$ and the angle s of rotation of the equivalent rotation operation. This is:

$$\hat{U}_n(s) = \exp\left(-i\frac{s}{2}\vec{\sigma}\cdot\vec{n}(\theta_n,\phi_n)\right), \qquad (4.4)$$

where $\vec{n}(\theta_n, \phi_n) = (\sin\theta_n\cos\phi_n, \sin\theta_n\sin\phi_n, \cos\theta_n)$ and θ_n, ϕ_n are the azimuthal and polar angles of $\vec{n}$ on the Poincaré sphere, respectively.

As mentioned before, our aim is to follow completely arbitrary paths on ray space. This is achieved by starting at an elliptically polarized state (from now on we replace $s_1 \to 0$ and $s_2 \to s_f$):

$$\rho(0) = |\psi(0)\rangle\langle\psi(0)| = \frac{1}{2}\left(\mathbb{1} + \vec{m}_0\cdot\vec{\sigma}\right), \qquad (4.5)$$

where $\mathbb{1}$ is the identity operator and $\vec{m}_0 = (\sin\theta_0\cos\phi_0, \sin\theta_0\sin\phi_0, \cos\theta_0)$ represents $\rho(0)$ on the Poincaré sphere.

Then, any curve C_0 given by $|\psi(s)\rangle\langle\psi(s)|, s \in [0, s_f]$ can be approximated by submitting $|\psi(0)\rangle$ to a series of rotations $\hat{U}_{n_k}(\Delta s_k), k = 1, ...N$ one after the other, so that in the limit $N \to \infty, \Delta s_k \approx \text{length}[C_0]/N \to ds$ the collection of geodesic arcs approximates C_0.

Even though what we have said before may serve to generate any curve $C_0 \subset \mathcal{R}_0$, for practical reasons and for the experimental implementation we will do our calculations related only to curves that arise from the rotation of an initial state around one single direction $\vec{n}$, which combined with the gauge gives us the most general $|\psi(s)\rangle$.[1] We will use:

$$|\psi(s)\rangle = e^{i\alpha(s)}\hat{U}_n(s)|\psi(0)\rangle. \tag{4.6}$$

Now, in order to make $\Phi_{dyn} = 0$ locally we need to ensure that $\langle\psi(s)|\dot{\psi}(s)\rangle = 0$, with $|\psi(s)\rangle$ given by Eq. 4.6. This leads to:

$$\dot{\alpha}(s) + \text{Im}\langle\psi(0)|\hat{U}_n^\dagger(s)\dot{\hat{U}}_n(s)|\psi(0)\rangle = 0. \tag{4.7}$$

Therefore, using Eq. (4.4), given an initial state $|\psi(0)\rangle$ and an axis of rotation $\vec{n}$, the gauge $\alpha(s)$ should be chosen such that:

$$\dot{\alpha}(s) = \frac{1}{2}\langle\psi(0)|\vec{\sigma}\cdot\vec{n}|\psi(0)\rangle, \tag{4.8}$$

and taking $\alpha(0) = 0$ we have

$$\alpha(s) = \frac{s}{2}\langle\psi(0)|\vec{\sigma}\cdot\vec{n}|\psi(0)\rangle. \tag{4.9}$$

4.2 Interferometric Calculations

In this section we discuss and calculate the particular intensity I from which we can extract the geometric phase $\Phi_g(s)$ acquired along $\rho(s) = \hat{U}_n(s)|\psi(0)\rangle\langle\psi(0)|\hat{U}_n^\dagger(s)$ with a similar method to the one exposed in Section 3.2.

In general, the initial state is elliptically polarized[2] $|\psi(0)\rangle = |E\rangle$. Then $\Phi_g(s)$ can be extracted from the intensity that arises from making $e^{i\alpha(s)}\hat{U}_n(s)|E\rangle$ and $|E\rangle$

[1] $|\widetilde{\psi}(s)\rangle$ is not used anymore. Instead, we use $|\psi(s)\rangle$ and $\langle\psi(s)|\dot{\psi}(s)\rangle = 0$ will give us a relation similar to Eq. 4.3

[2] From now on $|E\rangle$ represents an arbitrary elliptically polarized state.

interfere with each other, as we see below:

$$\begin{aligned} I &= \left| e^{i\mu}|E\rangle + e^{i\alpha(s)}\hat{U}_n(s)|E\rangle \right|^2 \\ &\propto 1 + |\,\langle E|\,\hat{U}_n(s)\,|E\rangle\,|\cos\left(\mu - \arg\langle E|\,e^{i\alpha(s)}\hat{U}_n(s)\,|E\rangle\right), \end{aligned} \tag{4.10}$$

where the phase μ appears due to the optical path difference between the arms of the interferometer used to get I. From Eq. (3.11) we find that the visibility is in general:

$$v = |\,\langle E|\,\hat{U}_n(s)\,|E\rangle\,|. \tag{4.11}$$

Now, using Eq. (4.9) we see that Φ_{dyn} vanishes, $\Phi_p = \Phi_g$, then:

$$\begin{aligned} \Phi_g &= \arg\langle E|\,e^{i\alpha(s)}\hat{U}_n(s)\,|E\rangle \\ &= \alpha(s) + \arg\langle E|\,\hat{U}_n(s)\,|E\rangle \\ &= \frac{s}{2}\langle E|\vec{\sigma}\cdot\vec{n}|E\rangle + \arg\langle E|\,\hat{U}_n(s)\,|E\rangle\,. \end{aligned} \tag{4.12}$$

Such an expression is useful if we work with states and operators. It helps to visualize these states and rotations on the Poincaré sphere. Then, it is worth having a relation that involves the vectors $\vec{m}_0$ and $\vec{n}$. A straightforward calculation leads us to:

$$\alpha(s) = \frac{s}{2}\vec{m}_0\cdot\vec{n}, \tag{4.13}$$

$$\arg\langle E|\hat{U}_n(s)|E\rangle = -\arctan\left(\tan\left(\frac{s}{2}\right)\vec{m}_0\cdot\vec{n}\right), \tag{4.14}$$

and accordingly:

$$\Phi_g = \frac{s}{2}\vec{m}_0\cdot\vec{n} - \arctan\left(\tan\left(\frac{s}{2}\right)\vec{m}_0\cdot\vec{n}\right), \tag{4.15}$$

which is the geometric phase[3] accumulated along the curve $\vec{m}(s)$ given by[4]:

$$\vec{m}(s) = \cos(s)\vec{m}_0 + (1-\cos(s))\,(\vec{m}_0\cdot\vec{n})\,\vec{n} + \sin(s)\,(\vec{n}\times\vec{m}_0)\,, \tag{4.16}$$

Finally, using Eqs. (4.10), (4.11) and (4.12) I reads:

$$I \propto 1 + v\cos\left(\mu - \Phi_g\right). \tag{4.17}$$

Just like in the case of measuring the Pancharatnam's phase, also here we want

[3]Naturally, Eq. (4.15) is valid as long as we are careful with the discontinuity of $\tan(s/2)$ and ensure that Φ_g is a smooth function of s.

[4]Eqs. (4.13)-(4.15) hold true in general and are valid for both the interferometric and polarimetric approaches.

to avoid any sort of perturbation to the experimental setup and isolate our measurements from external disturbances. We use the same strategy explained in Section (3.2). We need to find a way to obtain another intensity pattern $I_\perp$:

$$I_\perp \propto 1 + v\cos\left(\mu + \Phi_g\right), \tag{4.18}$$

so that we can extract the geometric phase Φ_g by measuring the relative shift between I and $I_\perp$ being twice Φ_g.

Eq. (4.18) is obtained from letting $e^{-i\alpha(s)}\hat{U}_n(s)|E_\perp\rangle$ and $|E_\perp\rangle$ interfere, with $|E_\perp\rangle$ a state orthogonal to $|E\rangle$:

$$\begin{aligned} I_\perp &= \left|e^{i\mu}|E_\perp\rangle + e^{-i\alpha(s)}\hat{U}_n(s)|E_\perp\rangle\right|^2 \\ &\propto 1 + |\langle E_\perp|\hat{U}_n(s)|E_\perp\rangle|\cos\left(\mu - \arg\langle E_\perp|e^{-i\alpha(s)}\hat{U}_n(s)|E_\perp\rangle\right) \\ &\propto 1 + |\langle E_\perp|\hat{U}_n(s)|E_\perp\rangle|\cos\left(\mu - \left(-\alpha(s) + \arg\langle E_\perp|\hat{U}_n(s)|E_\perp\rangle\right)\right), \end{aligned} \tag{4.19}$$

It can be shown that the following relations hold:

$$|\langle E_\perp|\hat{U}_n(s)|E_\perp\rangle| = |\langle E|\hat{U}_n(s)|E\rangle|, \tag{4.20}$$

$$\arg\langle E_\perp|\hat{U}_n(s)|E_\perp\rangle = -\arg\langle E|\hat{U}_n(s)|E\rangle. \tag{4.21}$$

Using such relations and Eqs. (4.11) and (4.12):

$$I_\perp \propto 1 + |\langle E|\hat{U}_n(s)|E\rangle|\cos\left(\mu + \left(\alpha(s) + \arg\langle E|\hat{U}_n(s)|E\rangle\right)\right). \tag{4.22}$$

Finally, $I_\perp$ reads:

$$I_\perp \propto 1 + v\cos(\mu + \Phi_g). \tag{4.23}$$

Now, let us focus on the implementation of the states and operators used to obtain I and $I_\perp$. To begin with, given an initial linear state, say $|H\rangle$, any elliptically-polarized state can be obtained by submitting $|H\rangle$ to the action of a quarter-wave plate followed by a half-wave plate. This will place the state on some plane on the Poincaré sphere (shown schematically in Fig. (4.2)) parallel to the equator ($x-y$ plane). The QWP fixes θ_0 as $\vec{m}_0 = (\sin\theta_0\cos\phi_0, \sin\theta_0\sin\phi_0, \cos\theta_0)$ and ϕ_0 is controlled by the argument of the HWP, where $\vec{m}_0$ points towards the projection of $|E\rangle$ on the Poincaré sphere. It can be shown that the arguments of the QWP and HWP needed to generate the state $|E\rangle$ that projects onto $|E\rangle\langle E| = \frac{1}{2}(\mathbb{1} + \vec{m}_0.\vec{\sigma})$

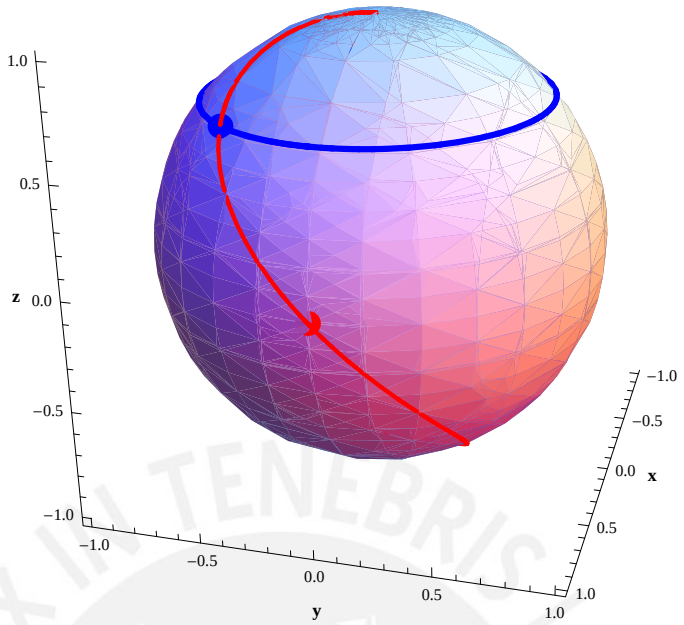

Figure 4.2: Any point on the Poincaré sphere can be reached by submitting a horizontally polarized state (red point at $\vec{m}_0 = (1, 0, 0)$) to the action of a QWP followed by a HWP: $\hat{H}(\theta_h)\hat{Q}(\theta_q)|H\rangle$. $\theta_h = 0$, $\theta_q \in [-\pi/4, \pi/4]$ projects onto the red curve and once fixed θ_q (blue point) the blue curve is reached by varying θ_h ($\theta_q = \pi/9$).

are given by:

$$\begin{aligned} |E\rangle &= \hat{H}\left(-\frac{\pi}{8} + \frac{\theta_0 + \phi_0}{4}\right)\hat{Q}\left(\frac{\pi}{4} + \frac{\theta_0}{2}\right)|H\rangle \\ &\equiv \hat{U}_{EH}|H\rangle. \end{aligned} \tag{4.24}$$

If we want to implement $\hat{U}_n(s)$ three waveplates $\hat{Q}\hat{H}\hat{Q}$ are enough since we already gave a recipe to generate any $\hat{U} \in SU(2)$ (see Eq. (3.7)). That would require to find how the arguments of the retarders and the parameters of $\hat{U}_n(s)$ are related to each other. This involves nonlinear relations. It is preferable to use a set of retarders that generates $\hat{U}_n(s) = \exp\left(-i\frac{s}{2}\vec{\sigma}\cdot\vec{n}(\theta_n, \phi_n)\right)$ in such a way that once we fix θ_n and ϕ_n the rotation can be generated by rotating a single wave plate. Such

an array is the following:

$$\begin{aligned}\hat{U}_n(s) &= \exp\left(-i\frac{s}{2}\vec{\sigma}.\vec{n}(\theta_n,\phi_n)\right)\\ &= \hat{Q}\left(\frac{\pi+\phi_n}{2}\right)\hat{Q}\left(\frac{\theta_n+\phi_n}{2}\right)\hat{H}\left(\frac{-\pi+\theta_n+\phi_n}{2}+\frac{s}{4}\right)\\ &\quad\times\hat{Q}\left(\frac{\theta_n+\phi_n}{2}\right)\hat{Q}\left(\frac{\phi_n}{2}\right),\end{aligned} \tag{4.25}$$

where we can see that if we fix the axis of rotation $\vec{n}(\theta_n,\phi_n)$ then the angles of the four QWP's are fixed while the angle of rotation s can be varied by rotating the HWP. Now we only need to define the optical implementation of the $U(1)$ elements $e^{i\alpha(s)}$ and $e^{-i\alpha(s)}$.

In order to generate the action of $e^{i\alpha(s)}$ on $\hat{U}_n(s)|E\rangle$ we may use some optical element that works as a phase shifter inside the interferometer, for example, a piece of glass, and then characterize the phase shift as function of its tilt. However, our setup, being insensitive to perturbations, requires that we use two co-propagating orthogonally polarized beams that pass through the same optical elements. Thus, it would be complicated to place two small pieces of glass on the path of each beam, one for $e^{i\alpha(s)}|E\rangle$ and the other for $e^{-i\alpha(s)}|E_\perp\rangle$, and independently manipulate both of them.

Alternatively, we may use a piezo-transducer to move the mirrors of the interferometer back and forth to change the optical-path difference between its arms. With this, we could control the relative phase between the interfering states and perform the action of $e^{i\alpha(s)}$. However, this would affect the two co-propagating beams equally and would implement $e^{i\alpha(s)}|E\rangle$ and $e^{i\alpha(s)}|E_\perp\rangle$ instead of what we need, such an array generates I but does not generate $I_\perp$.

In either case, what exposed above is neither efficient nor easy to implement and may introduce experimental errors significantly bigger than those due to other optical elements. At this point we came up with a very simple idea that once on the table appears to be the most immediate and obvious way to do. We just used more wave plates, which are elements of $SU(2)$, to perform $U(1)$ transformations. We can see that this works by noticing that

$$\exp\left(i\alpha(s)\vec{\sigma}\cdot\vec{n}_E\right)|E\rangle = e^{i\alpha(s)}|E\rangle, \tag{4.26}$$

$$\exp\left(i\alpha(s)\vec{\sigma}\cdot\vec{n}_E\right)|E_\perp\rangle = e^{-i\alpha(s)}|E_\perp\rangle, \tag{4.27}$$

where $\vec{n}_E$ corresponds to $|E\rangle\langle E|$ and $\exp(i\alpha(s)\vec{\sigma}\cdot\vec{n}_E)$ can be built using Eq. (4.25) with $s/2 \to -\alpha(s)$. Therefore, we can carry out the implementation of elements

$U(1)$ as given in Eqs. (4.26) and (4.27) by using a $SU(2)$ transformation such that the incoming states are its eigenstates. This would imply to use 5 retarders, but the lower the number of wave plates used the smaller the experimental errors. Accordingly, using Eq. (4.24), we can perform $e^{i\alpha(s)}|E\rangle$ by:

$$\begin{aligned} e^{i\alpha(s)}|E\rangle &= \hat{U}_{EH} e^{i\alpha(s)}|H\rangle \\ &= \hat{U}_{EH} \exp(i\alpha(s)\hat{\sigma}_x)|H\rangle \\ &= \hat{U}_{EH}\hat{Q}\left(-\frac{\pi}{4}\right)\hat{H}\left(\frac{\pi}{4}+\frac{\alpha(s)}{2}\right)\hat{Q}\left(-\frac{\pi}{4}\right)|H\rangle \\ &\equiv \hat{U}_{EH}\hat{U}_{\alpha(s)}|H\rangle. \end{aligned} \tag{4.28}$$

Hence, Eqs. (4.24)-(4.28) give us the recipe to generate the intensities I and $I_\perp$ (see Eqs. (4.17) and (4.23)) from which we can extract the geometric phase $\Phi_g(s)$ acquired along $\vec{m}(s)$ (see Eq. (4.16)). The most general interferometric setup needed to measure $\Phi_g(s)$ for an arbitrary $\vec{m}(s)$ is shown schematically in Fig. (4.3). It requires 12 retarders. As our aim is to show the versatility of our method, we have performed measurements for restricted non-geodesic curves such that significantly reduce the number of wave plates employed.

The first kind of curves arises from taking as the initial point $|H\rangle\langle H|$ and rotating it around an axis that lies on the equatorial plane of the Poincaré sphere (x-y plane). We have thus $\vec{m}_0 = (1,0,0)$ and $\vec{n} = (\cos\phi_n, \sin\phi_n, 0)$. Using Eq. (4.15) $\Phi_g^{\theta_n=\pi/2}(s)$ is plotted for some values of ϕ_n in Fig. (4.4) and is given by:

$$\Phi_g^{\theta_n=\pi/2}(s) = \frac{s}{2}\cos\phi_n - \arctan\left(\tan\frac{s}{2}\cos\phi_n\right). \tag{4.29}$$

For such a case only 6 retarders are needed because the $\hat{U}_{EH}$ in each arm of the interferometer are no longer required and $\hat{U}_n$ can be reduced to

$$\begin{aligned} \hat{U}_n^{\theta_n=\pi/2} &= \exp\left(-i\frac{s}{2}(\cos\phi_n\hat{\sigma}_x + \sin\phi_n\hat{\sigma}_y)\right) \\ &= \hat{Q}\left(-\frac{\pi}{4}+\frac{\phi_n}{2}\right)\hat{H}\left(\frac{\pi}{4}+\frac{\phi_n}{2}-\frac{s}{4}\right)\hat{Q}\left(-\frac{\pi}{4}+\frac{\phi_n}{2}\right). \end{aligned} \tag{4.30}$$

The $U(1)$ implementation is given by (see Eqs. (4.13) and (4.28)):

$$\hat{U}_{\alpha(s)}^{\theta_n=\pi/2} = \hat{Q}\left(-\frac{\pi}{4}\right)\hat{H}\left(\frac{\pi}{4}+\frac{s}{4}\cos\phi_n\right)\hat{Q}\left(-\frac{\pi}{4}\right). \tag{4.31}$$

In the second type of curves that we used for our measurements we took an arbitrary elliptically-polarized state $|E\rangle\langle E|$ as the initial state but constrained its evolution to a non-geodesic circle contained in a plane parallel to the equator. In

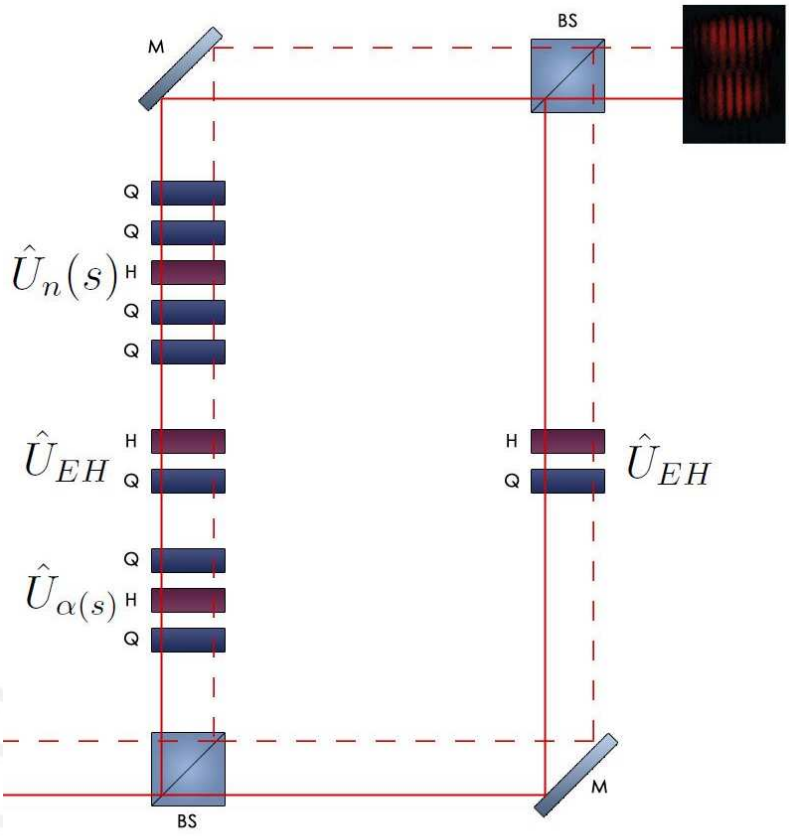

Figure 4.3: Interferometric arrangement for testing Geometric phase Φ_g. A light beam from a He-Ne laser is expanded and enters the interferometer by the left input with its lower and upper halves horizontally (continuous line) and vertically (dashed line) polarized, respectively. The left arm implements $\hat{U}_n(s)\hat{U}_{EH}(s)\hat{U}_{\alpha(s)}|H\rangle = e^{i\alpha(s)}|E(s)\rangle$ and $\hat{U}_n(s)\hat{U}_{EH}(s)\hat{U}_{\alpha(s)}|V\rangle = e^{-i\alpha(s)}|E_\perp(s)\rangle$ while the right one does $e^{i\mu}\hat{U}_{EH}(0)|H\rangle = e^{i\mu}|E(0)\rangle$ and $e^{i\mu}\hat{U}_{EH}(0)|V\rangle = e^{i\mu}|E_\perp(0)\rangle$. A CCD camera is placed at one of the outputs to capture the interference patterns $I \propto 1 + v\cos(\mu - \Phi_g)$ and $I_\perp \propto 1 + v\cos(\mu + \Phi_g)$ simultaneously, from which Φ_g is measured with an image-processing.

such a case $\vec{n} = (0, 0, 1)$ and $\vec{m}_0 = (\sin\theta_0\cos\phi_0, \sin\theta_0\sin\phi_0, \cos\theta_0)$, using again Eq. (4.15) we obtain this time for $\Phi_g^{\theta_n=0}(s)$:

$$\Phi_g^{\theta_n=0}(s) = \frac{s}{2}\cos\theta_0 - \arctan\left(\tan\frac{s}{2}\cos\theta_0\right), \tag{4.32}$$

which has the same structure of Eq. (4.29) and does not depend on the azimuthal coordinate of the initial state. In order to obtain $\Phi_g^{\theta_n=0}(s)$ an explicit implementation of $\hat{U}_n$ is not needed and we require only 7 retarders: 3 and 2 wave plates ($\hat{Q}\hat{H}\hat{Q}$ and $\hat{H}\hat{Q}$ respectively) in one arm of the interferometer for $e^{i\alpha(s)}|E(s)\rangle$ and 2 wave

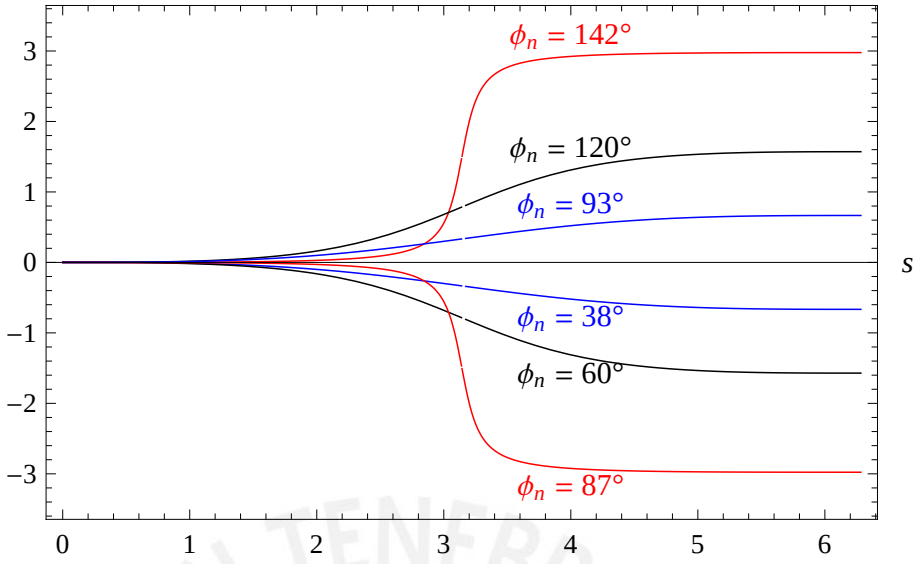

Figure 4.4: Geometric phase $\Phi_g^{\theta_n=\pi/2}(s)$ accumulated along a curve given by the rotation of $\vec{m}_0 = (1,0,0)$ around an axis $\vec{n} = (\cos\phi_n, \sin\phi_n, 0)$ being s the angle of rotation.

plates ($\hat{H}\hat{Q}$) on the other arm for $|E(0)\rangle$. Using Eqs. (4.24) and (4.28), we see that $e^{i\alpha(s)}|E(s)\rangle$ is given by:

$$\begin{aligned} e^{i\alpha(s)}|E(s)\rangle &= \hat{H}\left(-\frac{\pi}{8}+\frac{\theta_0+\phi_0}{4}+\frac{s}{4}\right)\hat{Q}\left(\frac{\pi}{4}+\frac{\theta_0}{2}\right) \\ &\times\hat{Q}\left(-\frac{\pi}{4}\right)\hat{H}\left(\frac{\pi}{4}+\frac{s}{4}\cos\theta_0\right)\hat{Q}\left(-\frac{\pi}{4}\right)|H\rangle. \end{aligned} \tag{4.33}$$

In Section 4.4.1 we show the results of our measurements of Φ_g. Let us first turn to the calculations involved in the polarimetric approach.

4.3 Polarimetric Calculations

In this section we discuss the polarimetric method to measure Φ_g. Just like we did in Section 3.3, in order to avoid an excessive number of wave plates in the experimental setup we will make our calculations considering an initial linear-polarized state, say $|H\rangle$.

As we discussed before, the polarimetric method consists on building a state $|S\rangle = \frac{1}{\sqrt{2}}(|H\rangle - ie^{i\mu}|V\rangle)$ by introducing a relative phase μ[5] between the initial state and its orthogonal state (see Eq. (3.33)). We then apply the evolution operator to

[5]This phase has the role of the phase due to the optical-path difference between the arms of an interferometer.

obtain:

$$\hat{U}|S\rangle = \frac{1}{\sqrt{2}}\left(\hat{U}|H\rangle - ie^{i\mu}\hat{U}|V\rangle\right), \tag{4.34}$$

and finally project such state onto $|S\rangle$, thereby obtaining an intensity patter from which maxima and minima with respect to μ give us information of the accumulated total phase Φ_P.

Now, in our case, where $\Phi_p = \Phi_g$, the evolving state is $e^{i\alpha(s)}\hat{U}_n(s)|H\rangle$ ($\alpha(s)$ as given in Eq. (4.13)), hence, Eq. (4.34) must be changed to:

$$\hat{U}_n(s)|S\rangle = \frac{1}{\sqrt{2}}\left(e^{i\alpha(s)}\hat{U}_n(s)|H\rangle - ie^{i\mu}\hat{U}_n(s)|V\rangle\right), \tag{4.35}$$

and we should be able to obtain Φ_g from measurements of the maximal and minimal intensity:

$$I = |\langle S|\hat{U}_n(s)|S\rangle|^2. \tag{4.36}$$

To show that this is the case, we use $\hat{U}_n(s)$ as given in Eq. (4.4) to explicitly calculate I. A straightforward calculation gives:

$$\begin{aligned} I &= \cos^2\left(\frac{s}{2}\right) + \sin^2\left(\frac{s}{2}\right)[\cos(\theta_n)\cos\left(\mu - \alpha(s)\right) \\ &\quad - \sin(\theta_n)\sin(\phi_n)\sin\left(\mu - \alpha(s)\right)]^2, \end{aligned} \tag{4.37}$$

which has its minimum and maximum values with respect to μ at:

$$I_{\min} = \cos^2\frac{s}{2}, \tag{4.38}$$

$$I_{\max} = \cos^2\frac{s}{2} + \sin^2\frac{s}{2}\left(\cos^2\theta_n + (\sin\theta_n\sin\phi_n)^2\right). \tag{4.39}$$

Using Eqs. (4.38) and (4.39) we can build the following expressions:

$$\frac{1 - I_{\max}}{1 - I_{\min}} = (\sin\theta_n\cos\phi_n)^2, \tag{4.40}$$

$$\frac{1 - I_{\max}}{I_{\min}} = \left(\tan\frac{s}{2}\sin\theta_n\cos\phi_n\right)^2. \tag{4.41}$$

Now, noticing that the geometric phase Φ_g for this case, i.e., $\vec{m}_0 = (1, 0, 0)$ and $\vec{n} = (\sin\theta_n\cos\phi_n, \sin\theta_n\sin\phi_n, \cos\theta_n)$, is given by (see Eq. 4.15):

$$\Phi_g^{\text{pol}}(s) = \frac{s}{2}\sin\theta_n\cos\phi_n - \arctan\left(\tan\frac{s}{2}\sin\theta_n\cos\phi_n\right), \tag{4.42}$$

and using Eqs. (4.38), (4.40) and (4.41) we conclude that Φ_g^{pol} can be measured

through:

$$\Phi_g^{\text{pol}} = \arccos\left(\sqrt{I_{\min}}\right)\sqrt{\frac{1-I_{\max}}{1-I_{\min}}} - \arctan\left(\sqrt{\frac{1-I_{\max}}{I_{\min}}}\right). \tag{4.43}$$

This expression is zero $\forall s$ for two cases: $\vec{m}_0 \cdot \vec{n} = 1$ (entire evolution restricted to the same point $\vec{m}_0 = (1,0,0)$ on ray space) and $\vec{m}_0 \cdot \vec{n} = 0$ (great circles on ray space).

What we need to do now is to find the particular set of wave plates and projectors that generate I as given by Eq. (4.37). To do this, we look back to Eq. (4.35) and notice that the state

$$|S\rangle = \frac{1}{\sqrt{2}}\left(e^{i\alpha(s)}|H\rangle - ie^{i\mu}|V\rangle\right) \tag{4.44}$$

is, up to a physically irrelevant global phase factor, equal to

$$\begin{aligned}
|S\rangle &= \frac{e^{-i(\mu+\alpha(s))/2}}{\sqrt{2}}\left(e^{i\alpha(s)}|H\rangle - ie^{i\mu}|V\rangle\right) \\
&= \frac{1}{\sqrt{2}}\left(e^{-i(\mu-\alpha(s))/2}|H\rangle - ie^{i(\mu-\alpha(s))/2}|V\rangle\right) \\
&= \exp\left(-i\left(\frac{\mu-\alpha(s)}{2}\right)\hat{\sigma}_x\right)\left(\frac{1}{\sqrt{2}}\left(|H\rangle - i|V\rangle\right)\right) \\
&= \exp\left(-i\left(\frac{\mu-\alpha(s)}{2}\right)\hat{\sigma}_x\right)\exp\left(-i\frac{\pi}{4}\hat{\sigma}_y\right)|H\rangle.
\end{aligned} \tag{4.45}$$

Hence, I may be obtained from (see Eq. (4.36)):

$$\begin{aligned}
I &= \left|\langle H|\hat{U}_{tot}|H\rangle\right|^2 \\
&= \left|\langle H|\exp\left(i\frac{\pi}{4}\hat{\sigma}_y\right)\exp\left(i\left(\frac{\mu-\alpha(s)}{2}\right)\hat{\sigma}_x\right)\right. \\
&\quad \left.\times\hat{U}_n(s)\exp\left(-i\left(\frac{\mu-\alpha(s)}{2}\right)\hat{\sigma}_x\right)\exp\left(-i\frac{\pi}{4}\hat{\sigma}_y\right)|H\rangle\right|^2.
\end{aligned} \tag{4.46}$$

Using Eqs. (3.42)-(3.44) we can implement the total operator appearing in the last equation as:

$$\begin{aligned}
\hat{U}_{tot} &= \hat{H}\left(-\frac{\pi}{4}\right)\hat{H}\left(\frac{\mu-\alpha(s)+\pi}{4}\right)\hat{Q}\left(-\frac{\pi}{4}\right) \\
&\quad \times\hat{U}_n(s)\hat{Q}\left(\frac{\pi}{4}\right)\hat{H}\left(\frac{\mu-\alpha(s)-\pi}{4}\right)\hat{H}\left(\frac{\pi}{4}\right).
\end{aligned} \tag{4.47}$$

However, with $\hat{U}_n(s)$ as given in Eq. (4.25), $\hat{U}_{tot}$ would require to employ eleven retarders. This number can be reduced using relations like Eqs. (3.46) and (3.47)

to finally find the array of seven wave plates that we used in our measurements:

$$\begin{aligned}\hat{U}_{tot}(\theta_n,\phi_n,s,\mu) \;=\; & \hat{Q}\left(\frac{\pi}{4}+\frac{s}{4}\sin\theta_n\cos\phi_n-\frac{\mu}{2}\right)\\ & \times\hat{Q}\left(-\pi-\frac{\phi_n}{2}+\frac{s}{4}\sin\theta_n\cos\phi_n-\frac{\mu}{2}\right)\\ & \times\hat{Q}\left(\frac{\pi}{2}-\frac{\theta_n+\phi_n}{2}+\frac{s}{4}\sin\theta_n\cos\phi_n-\frac{\mu}{2}\right)\\ & \times\hat{H}\left(-\frac{\theta_n+\phi_n}{2}-\frac{s}{4}+\frac{s}{4}\sin\theta_n\cos\phi_n-\frac{\mu}{2}\right)\\ & \times\hat{Q}\left(\frac{\pi}{2}-\frac{\theta_n+\phi_n}{2}+\frac{s}{4}\sin\theta_n\cos\phi_n-\frac{\mu}{2}\right)\\ & \times\hat{Q}\left(\frac{\pi}{2}-\frac{\phi_n}{2}+\frac{s}{4}\sin\theta_n\cos\phi_n-\frac{\mu}{2}\right)\\ & \times\hat{Q}\left(-\frac{\pi}{4}+\frac{s}{4}\sin\theta_n\cos\phi_n-\frac{\mu}{2}\right),\end{aligned}\tag{4.48}$$

where we have explicitly written $\alpha(s)=(s/2)\cos\theta_n\sin\phi_n$ and $\hat{U}_{tot}$ is given in such a way that once we have rotated $\vec{m}_0=(1,0,0)$ around some $\vec{n}$ by an angle of s radians, i.e., fixing θ_n,ϕ_n and s, we can run μ by rotating the entire set of retarders with the help of some mechanical apparatus, thereby obtaining $I_{\min}$ and $I_{\max}$, and therefore $\Phi_g(s)$ (see Eq. 4.43). The experimental setup that we used in our measurements of Φ_g by the polarimetric method is similar to the one in Fig. (3.3) but with seven wave plates instead of five.

The results of our measurements for both the interferometric and polarimetric methods are shown in the next section.

4.4 Experimental Procedures and Results

The experimental setup for measuring geometric phases is a modification of the one used for the Pancharatnam's phase measurements (it is the same with more retarders). The experimental procedures in this section are therefore analogous to those discussed in Section (3.4). Below we present the results of our measurements.

4.4.1 Interferometric Measurements

As we discussed in Section 4.2, we have performed measurements of the geometric phase Φ_g accumulated along two types of curves. The first type arises from rotating $\vec{m}_0=(1,0,0)$ around $\vec{n}=(\cos\phi_n,\sin\phi_n,0)$ by an angle of s radians. For such a case, $\Phi_g^{\theta_n=\pi/2}$ is given by Eq. (4.29).

Any circle on the Poincaré sphere can be given in terms of the unit vector $\vec{n}$ that goes through the center of the circle and the angle β between $\vec{n}$ and any point $\vec{m}_0$ on the circle ($\cos\beta = \vec{m}_0 \cdot \vec{n}$). β determines the solid angle Ω subtended by the circle through:

$$\Omega = 2\pi(1 - \vec{m}_0 \cdot \vec{n}). \tag{4.49}$$

Therefore, the well known relation between the geometric phase acquired in cyclic evolutions and the solid angle Ω, i.e., $\Phi_g = -\Omega/2$, implies that for a 2π rotation of $\vec{m}_0$ around $\vec{n}$:

$$\Phi_g(2\pi) = -\pi(1 - \vec{m}_0 \cdot \vec{n}), \tag{4.50}$$

which for our case ($\vec{m}_0 \cdot \vec{n} = \cos\phi_n$) reduces to:

$$\Phi_g^{\theta_n=\pi/2}(2\pi) = -\pi(1 - \cos\phi_n). \tag{4.51}$$

If we set $\phi_n = 60°$, then $\beta = 60°$ and $\Phi_g(2\pi) = -90°$. The path traced by the state and our measurements of Φ_g (given in degrees for a better visualization) are shown in Fig. (4.5). As we can see, Φ_g goes to $-90°$ as s approaches to 2π.

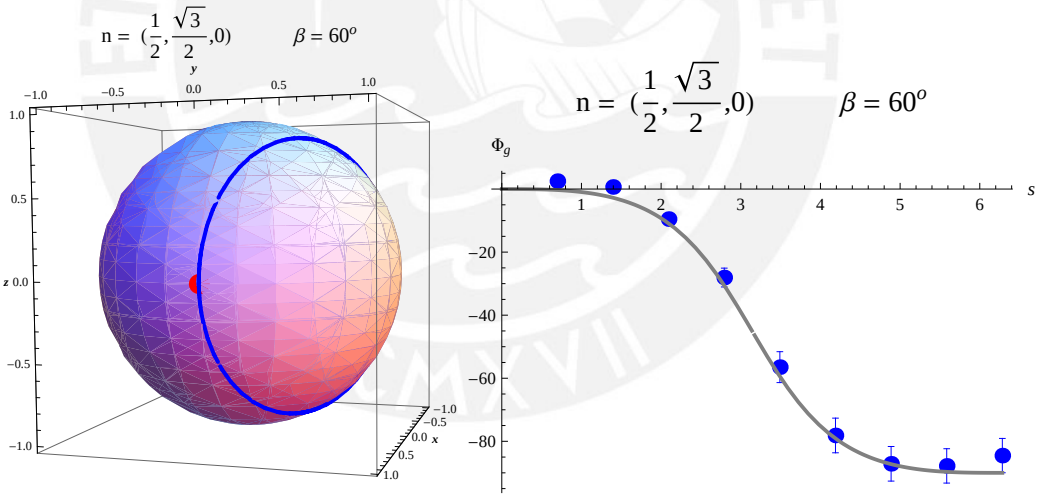

Figure 4.5: *Left*: Path traced on the Poincaré sphere by the polarization of light for $\theta_n = 90°$ and $\phi_n = 60°$. *Right*: Measurement of $\Phi_g^{\theta_n=\pi/2}$ for $\phi_n = 60°$.

The second type of curves is generated from rotating $\vec{m}_0$ around $\vec{n} = (0, 0, 1)$ by an angle of s radians. Hence, $\beta = \theta_0$. For measuring $\Phi_g^{\theta_n=0}$ (see Eq. (4.32)) we took $\theta_0 = \beta = 60°$. Again, $\Phi_g \to -90°$ as $s \to 2\pi$. Fig. (4.6) shows the path traced and the measurements of $\Phi_g^{\theta_n=0}$.

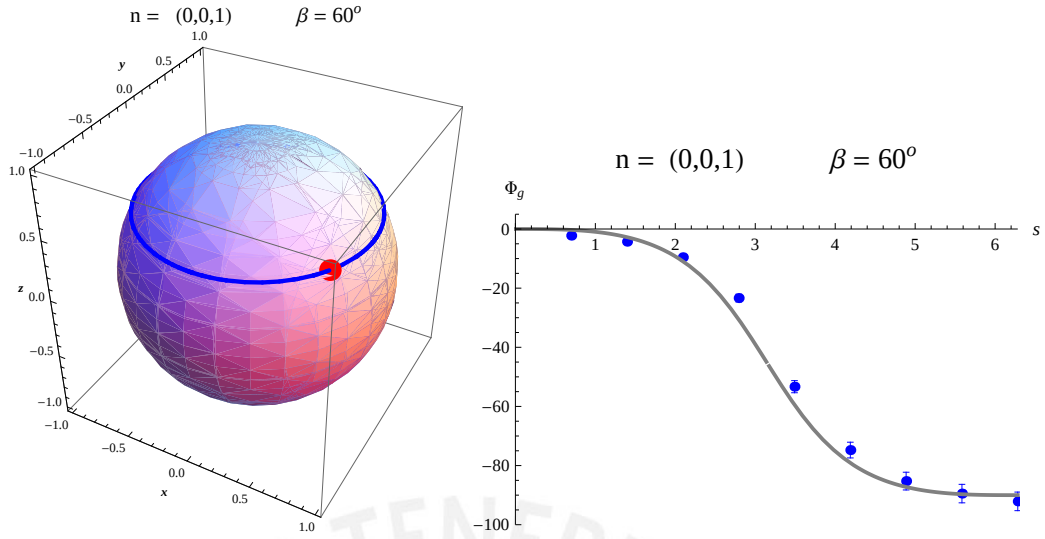

Figure 4.6: *Left*: Path on the Poincaré sphere traced by the polarization of light for $\theta_n = 0°$ and $\theta_0 = 60°$. *Right*: Measurement of $\Phi_g^{\theta_n=0}$ for $\theta_0 = 60°$.

4.4.2 Polarimetric Measurements

Measuring the geometric phase by the polarimetric method discussed in Section 4.3 does not impose a constraint for $\vec{n}$ but it does require the initial state to be

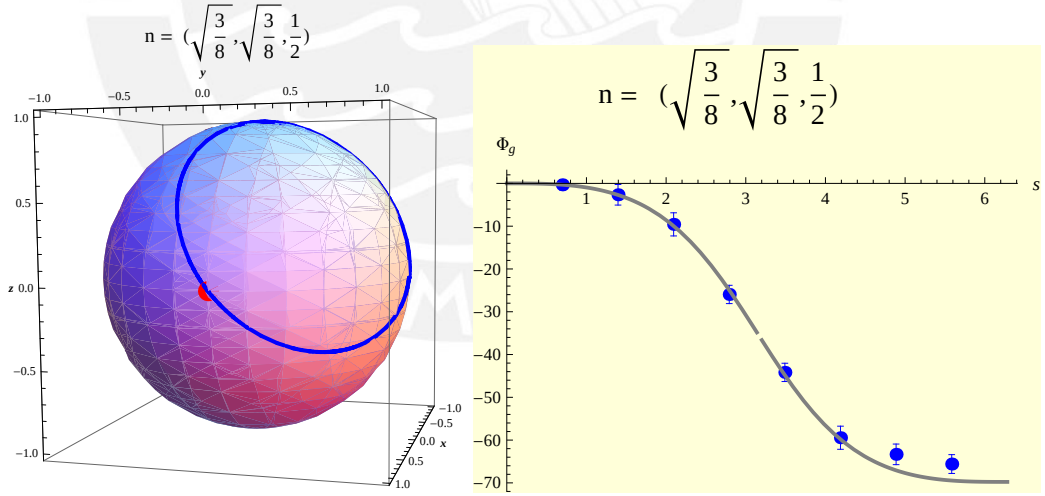

Figure 4.7: *Left*: Path on the Poincaré sphere traced by the polarization of light for $\theta_n = 60°$ and $\phi_n = 45°$. *Right*: Measurement of Φ_g^{pol} for $\theta_n = 60°$ and $\phi_n = 45°$.

$\vec{m}_0 = (1, 0, 0)$. We took $\theta_n = \pi/3$ and $\phi_n = \pi/4$ for our measurements of Φ_g^{pol} (see Eq. (4.42)), in which case $\beta \approx 52°$ ($\cos\beta = \vec{m}_0 \cdot \vec{n}$) and $\Phi_g \to\approx -70°$ as $s \to 2\pi$ (see Eq. (4.50)). The curve on the Poincaré sphere corresponding to this evolution and our measurements of Φ_g^{pol} are shown in Fig. (4.7).

The retarders and polarizers could be oriented to within 1°. As expected, the experimental results are within 3-7% in accordance with the theoretical predictions, depending on the number of wave plates being employed.

Chapter 5

Summary and Conclusions

In the first part of this thesis work (Chapter 3) we have carried out theoretical calculations and the corresponding measurements of Pancharatnam's phase by applying polarimetric and interferometric methods. In the second part (Chapter 4) we have given a recipe to make the dynamical component of the phase vanish and to measure geometric phases. Under the hypothesis of working with evolutions free of decoherence and polarized photons as isolated systems, our experimental findings were in very good agreement with the theoretical predictions.

Our interferometric setups are robust against thermal and mechanical disturbances, effectively isolating our interferometers from typical drawbacks. Our procedure can be implemented with a Michelson, a Sagnac or a Mach-Zehnder interferometer. We have compared interferometric measurements with those obtained with a polarimetric array, finding similar results in both cases. Our polarimetric arrays simply consisted of two polarizers and five (for measuring Pancharatnam's phase) or seven (for measuring geometric phases) wave-plates. The whole Poincaré sphere of polarization states could be explored with both our polarimetric and interferometric arrays.

Additionally, we have tested theoretical predictions concerning fringe visibility when applying the interferometric method, finding very good agreement with that expected theoretically. This is interesting not only on its own, but also in view of extracting quantum phases from visibility measurements in the case of mixed states. Indeed, it has been proved [18] that, for mixed states, fringe visibility is a simple function of Pancharatnam's phase.

An immediate extension of this work would aim at replacing the classical laser source by different single photon sources. Standard single qubit states or nonmaximally entangled states [27] could be used. We could then study and use geometric phases under decoherence effects.

Bibliography

[1] P. J. Leek, J. M. Fink, A. Blais, R. Bianchetti, M. Gppl, J. M. Gambeta, D. I. Schuster, L. Frunzio, R. J. Schoelkopf and A. Wallraff, "Observation of Berry's Phase in a Solide-State Qubit," *Science* **318** (2007) 1889.

[2] S. Fillipp, J. Klepp, Y. Hasegawa, C. Plonka-Spehr, U. Schmidt, P. Geltenbort and H. Rauch, "Experimental Demonstration of the Stability of Berry's Phase for a Spin 1/2 Particle," *Phys. Rev. Lett.* **102** 030404.

[3] Y. Ota, Y. Goto, Y. Kondo and M. Nakahara, "Geometric Quantum Gates in Liquid-State NMR based on a Cancellation of Dynamical Phases," *Phys. Rev. A* **80** 052311.

[4] S. Pancharatnam *Proc. Ind. Acad. Sci. A* **44** (1956) 247.

[5] M. V. Berry *Proc. R. Soc. London A* **392** (1984) 45.

[6] M. V. Berry *J. Mod. Opt.* **34** (1987) 1401.

[7] V. Bargmann, "Note on Wigner's Theorem on Symmetry Operations," *J. Math. Phys.* **5** (1964) 862–868.

[8] R. Simon and N. Mukunda, "Quantum Kinematic Approach to the Geometric Phase," *Annals of Physics* **228** (1993) 205–268.

[9] J. C. Loredo, O. Ortíz, R. Weingärtner and F. De Zela, "Measurement of Pancharatnam's phase by robust interferometric and polarimetric methods," *Phys. Rev. A* **80** (2009) 0121113.

[10] R. Simon and N. Mukunda, "Minimal three-component SU(2) gadget for polarization optics," *Phys. Lett. A* **143** (1990) 165.

[11] A.G. Wagh, V.C. Rakhecha, "On measuring the Pancharatnam phase. I. Interferometry," *Phys. Lett. A* **197** (1995) 107–111.

[12] Berthold-Georg Englert, Christian Kurtsiefer, and Harald Weinfurter, "Universal unitary gate for single-photon two-qubit states," *Phys. Rev. A* **63** (2001) 032303.

[13] W. P. Schleich, "Quantum Optics in Phase Space," *(Wiley-VCH, Berlin)* (2001) .

[14] A.G. Wagh, V.C. Rakhecha, "On measuring the Pancharatnam phase. II. $SU(2)$ polarimetry," *Phys. Lett. A* **197** (1995) 112–115.

[15] Peter Larsson, "Quantal Phases in Polarimetry," *Masters Thesis to Uppsala University* .

[16] K. A. Goldberg and J. Bokor, "Fourier-Transform Method of Phase-Shift Determination," *Appl. Opt.* **40** (2001) 2886.

[17] H. M. Wong, K. M. Cheng and M.-C. Chu, "Quantum Geometric Phase between Orthogonal States," *Phys. Rev. Lett.* **94** (2005) 070406.

[18] E. Sjöqvist, A. K. Pati, A. Ekert, J. S. Anandan, M. Ericsson, D. K. L. Oi, V. Vedral, "Geometric Phases for Mixed States in Interferometry," *Phys. Rev. Lett.* **85** (2000) 2845–2849.

[19] P. Zanardi and M. Rasetti, "Holonomic Quantum Computation," *Phys. Lett. A* **264** (1999) 94–99.

[20] A. Blais and A.-M.S. Tremblay, "Effect of Noise on Geometric Logic Gates for Quantum Computation," *Phys. Rev. A* **67** (2003) 012308.

[21] L.-M. Duan-, J. I. Cirac and P. Zoller, "Geometric Manipulation of Trapped Ions for Quantum Computation," *Science* **292** (2001) 1695.

[22] H. Kobayashi, S. Tamate, T. Nakanishi, K. Sugiyama and M. Kitano, "Direct Observation of Geometric Phases using a three-pinhole Interferometer," *Phys. Rev. A* **81** (2010) 012104.

[23] M. Ericsson, D. Achilles, J. T. Barreiro, D. Branning, N. A. Petters and P. G. Kwiat, "Measurement of Geometric Phase for Mixed States Using Single Photon Interferometry," *Phys. Rev. Lett.* **94** (2005) 050401.

[24] J. Anandan, "The Geometric Phase," *Nature* **360** (1992) 307–313.

[25] J. A. Jones, V. Vedral, A. Ekert and G. Castagnoli, "Geometric Quantum Computation using Nuclear Magnetic Resonance," *Nature* **403** (1999) 869–871.

[26] P. Solinas, P. Zanardi, N. Zanghi and F. Rossi, "Semiconductor-based Geometrical Quantum Gates," *Phys. Rev. B* **67** (2003) 121307.

[27] Andrew G. White, Daniel F. V. James, Philippe H. Eberhard and Paul Kwiat, "Nonmaximally Entangled States: Production, Characterization, and Utilization," *Phys. Rev. Lett.* **83** (1999) 3103–3107.